



Exploring Alternative SMAP Level-4 Carbon Model Formulations for the North American Arctic–Subarctic Growing Season

Rémi Madelon^{1,2,3}, K. Arthur Endsley⁴, John S. Kimball⁴, Gabrielle J. M. De Lannoy⁵, Oliver Sonnentag^{3,6}, Haley Alcock⁶, Alex Mavrović^{1,3,7}, Scott N. Williamson⁸, Vincent Maire^{1,3}, Arnaud Mialon², and Alexandre Roy^{1,3}

¹Université du Québec à Trois-Rivières (UQTR), Recherche en modélisation et télédétection des environnements nordiques (ReMoTE-Nord) group, Trois-Rivières, QC, Canada

²Univ Toulouse, CNES/IRD/CNRS/INRAe, CESBIO, Toulouse, France

³Centre d'Etudes Nordiques (CEN), Québec, QC, Canada

⁴University of Montana, Numerical Terradynamic Simulation Group (NTSG), Missoula, MT, United States

⁵Katholieke Universiteit Leuven (KU Leuven), Department of Earth and Environmental Sciences, Division Soil and Water Management, Leuven, Belgium

⁶Université de Montréal (UdeM), Département de Géographie, Montréal, QC, Canada

⁷Cégep de Sherbrooke, Physics Department, Sherbrooke, QC, Canada

⁸Polar Knowledge Canada, Cambridge Bay, NU, Canada

Correspondence: Rémi Madelon (remi.madelon@uqtr.ca or remi.madelon@utolouse.fr)

Abstract. The Soil Moisture Active Passive Level-4 Terrestrial Carbon Flux model (hereafter referred to as the L4C model) provides daily estimates of net ecosystem CO₂ exchange (NEE), gross primary production (GPP), and ecosystem respiration (ER) at a global scale. The model is based on direct mechanistic forcing–response relationships between CO₂ fluxes and energy proxies (absorbed photosynthetically active radiation and temperature) and moisture proxies (soil moisture and vapor pressure deficit). Although the L4C model aims to provide a representative estimation of the CO₂ budget of Arctic and Subarctic (AS) environments, a deeper understanding of carbon cycle processes and targeted refinements are needed to improve its accuracy. In this study, alternative model formulations are proposed for the North American AS regions during the growing season. These formulations are calibrated and evaluated using NEE-derived GPP and ER from 20 eddy covariance towers across western Canada and Alaska, covering the period from 2015 to 2022. Refinements in the representation of energy proxies resulted in greater improvements in model performance than adjustments to moisture proxies. Specifically, implementing a light-response curve in GPP estimation reduced unbiased root mean squared error and bias, while incorporating growing degree days improved correlation. Adjustments to rootzone and surface soil moisture in GPP and ER estimation, respectively, did not yield conclusive performance improvements. Vapor pressure deficit showed limited importance as a driver of GPP in upland tundra and wetlands, whereas it had a stronger impact in taiga forests. Finally, the litterfall scheme used to represent SOC dynamics in the L4C ER model formulation in version 8 demonstrated improved performance relative to version 7. These results highlight opportunities to enhance the accuracy of the L4C model for the North American AS growing season but also underscore the need for further research on ER modeling.



1 Introduction

Arctic and Subarctic (AS) environments store nearly half of the global soil organic carbon (SOC) pool (Tarnocai et al., 2009; 20 Hugelius et al., 2014; Mishra et al., 2021) and are experiencing accelerated warming (Rantanen et al., 2022). Rising temperatures increase photosynthetic activity and extend the growing season, leading to higher CO₂ uptake by vegetation (Myneni et al., 1997; Jia et al., 2003; Euskirchen, E. S. et al., 2009; Natali et al., 2012; Forkel et al., 2016; Fisher et al., 2018). In addition, rising temperatures enhance autotrophic respiration (AR) as well as heterotrophic respiration (HR) in two pathways: 25 directly, by stimulating microbial activity, and indirectly, by thawing permafrost and exposing frozen SOC to decomposition. The combined increase in AR and HR intensifies CO₂ release to the atmosphere (Natali et al., 2019; Turetsky et al., 2020; 30 Virkkala et al., 2024). Consequently, estimating the net CO₂ budget of AS regions is essential for understanding their role in global climate system feedbacks (Oechel et al., 1993; Hayes et al., 2011; Turetsky et al., 2011; Bell et al., 2013; Schuur et al., 2013; Schaefer et al., 2014; Zona et al., 2016). Nevertheless, our understanding of CO₂ fluxes in the AS environments remains limited. This is due to the inherent complexity and high cost of measuring CO₂ fluxes, the scarcity of such measurements, and 35 the seasonal variability in the dominant processes controlling CO₂ fluxes (Baldocchi et al., 2007; Fisher et al., 2018; Pallandt et al., 2022; Mavrovic et al., 2023b).

Net ecosystem CO₂ exchange (NEE) represents the overall balance between CO₂ uptake by photosynthesis, called gross primary production (GPP), and CO₂ release through ecosystem respiration (ER), as follows (Chapin et al., 2006)

$$\text{NEE} = \text{HR} + \text{AR} - \text{GPP} = \text{ER} - \text{GPP} \quad (1)$$

35 GPP is a light-driven process whose efficiency is modulated by air temperature, soil moisture availability within the plant root zone and vapor pressure deficit, which can induce stomatal closure and thereby reduce CO₂ uptake (Davis et al., 2014; Bao et al., 2022). Comparatively, HR is governed by SOC availability, soil temperature, and surface soil moisture, whereas AR primarily depends on air temperature, plant metabolic activity and GPP rate (Reichstein et al., 2005; Davis et al., 2014; Zona et al., 2023). When soil temperature drops near 0 °C, the soil starts freezing and GPP and AR progressively ceases, following 40 a soil freezing characteristic curve (Salmabadi et al., 2025). Under fully frozen conditions, NEE is equal to HR, which is controlled by soil temperature and SOC availability (Natali et al., 2019; Mavrovic et al., 2023b).

Although global terrestrial carbon flux (TCF) models, atmospheric inversions (which infer surface CO₂ fluxes from atmospheric CO₂ concentrations), and data-driven flux-upscaling approaches are available to estimate the CO₂ budget of AS regions, they often disagree on whether these regions are CO₂ sources or sinks (McGuire et al., 2012; Fisher et al., 2018; 45 López-Blanco et al., 2019; Virkkala et al., 2021; Ramage et al., 2024; Virkkala et al., 2024; Foster et al., 2024). In recent decades, satellite-based microwave remote sensing (300 MHz – 100 GHz) has provided a valuable approach for monitoring land-atmosphere interactions and carbon cycle dynamics through the retrieval of key surface variables (Fisher et al., 2018; Lees et al., 2018; Mavrovic et al., 2023a; Pulliainen et al., 2024) such as soil moisture (Kerr et al., 2012; Colliander et al., 2017), snow properties (Lievens et al., 2019), aboveground biomass (Mialon et al., 2020), and freeze-thaw state (Rautiainen et al., 2016; Derksen et al., 2017; Prince et al., 2019). In 2015, the Soil Moisture Active Passive (SMAP) satellite was launched 50 to monitor surface soil moisture and freeze-thaw dynamics using L-band brightness temperature observations (Entekhabi et al.,



2010). One of the science objectives of the SMAP mission is to improve our understanding of interconnected water, energy, and carbon cycles, as well as to quantify the boreal landscape CO₂ budget (Entekhabi et al., 2014). In this context, the SMAP Level-4 Global Daily 9-km EASE-Grid Carbon Net Ecosystem Exchange (SPL4CMDL) product currently provides global, 55 daily estimates of NEE and GPP, as well as ER (indirectly derived from HR, GPP and NEE). These estimates are derived from a TCF model (hereafter referred to as the L4C model), which is notably informed by the SMAP Level-4 Global 9-km EASE-Grid Surface and Root Zone Soil Moisture Geophysical Data (SPL4SMGP) product (Jones et al., 2017; Endsley et al., 2022; Kimball et al., 2025; Reichle et al., 2025). Although the L4C model achieves an unbiased root-mean-square error of NEE within the targeted accuracy of 1.6 gCm⁻²d⁻¹ in AS environments, recent studies have reported that it fails to capture 60 the amplitude of GPP and ER during the green-up phase (Endsley et al., 2022; Madelon et al., 2025). The authors also reported discrepancies in annual CO₂ budgets when compared with eddy covariance (EC) measurements, leading to uncertainties in classifying AS environments as net CO₂ sources or sinks (Madelon et al., 2025). From April to July 2025, the L4C model transitioned from version 7 to version 8 (Kimball et al., 2025), featuring a major update partly due to (i) the upgrade of the SMAP SPL4SMGP product, which transitioned from its own version 7 to version 8 (Reichle et al., 2025), and (ii) changes to 65 the litterfall estimation scheme used for modeling SOC dynamics and ER (Section 3).

The goal of this study is to better characterize how key environmental drivers influence GPP and ER, and to refine their modeling for the North American AS growing season. To achieve this, we:

- explore alternative formulations of the L4C model (hereafter referred to as the AS-adapted models) that adjust GPP and ER responses to absorbed photosynthetically active radiation, air and soil temperature, rootzone and surface soil moisture, and vapor pressure deficit;
- calibrate and evaluate these formulations using GPP and ER data from 20 EC towers across western Canada and Alaska from 2015 to 2022;
- identify and interpret the specific model adjustments that yield the greatest performance improvements in terms of Pearson correlation, unbiased root-mean-square error, and bias;
- 75 – provide recommendations for more accurate satellite-derived estimates of GPP and ER, with indirect benefits for NEE and CO₂ budget estimation.

2 Eddy covariance measurements

NEE, GPP, and ER data were collected from 20 EC towers located in AS environments (Figure 1), all within the NASA Arctic-Boreal Vulnerability Experiment (ABoVE) study domain (<https://above.nasa.gov/sites.html>). The dataset spans from 80 April 2015 through December 2022 (Table 1) and includes

- half-hourly fluxes from 13 EC towers in Alaska, downloaded from the AmeriFlux Network website (<https://ameriflux.lbl.gov>).



- half-hourly fluxes from 7 EC towers in western Canada, provided directly by the principal investigators to ensure the use of the most up-to-date records; some of these sites are not yet available on the AmeriFlux Network website.

EC towers measure NEE by quantifying the turbulent vertical exchange of CO₂ in the surface layer of the atmospheric boundary layer (typically within the lowest tens of meters), where turbulence dominates the airflow (Aubinet et al., 2012; Burba, 2013, 2022). The spatial footprint can extend up to 1 km or more, but remains complex to calculate and varies with wind direction, wind speed, and tower height (Leclerc and Thurtell, 1990; Schuepp et al., 1990; Aubinet et al., 2012; Webb et al., 2016). NEE measurements are subject to systematic errors, which mostly arise from unmet assumptions, instrument design and calibration, physical phenomena (e.g. storage terms), and terrain-specific conditions. These errors are generally well characterized and are typically corrected using software, such as EddyPro, as part of the standard flux processing workflow (Aubinet et al., 2012; Burba, 2022). NEE measurements are also affected by random errors, notably turbulence sampling error, which arises when large eddies are not adequately captured within a 30-minute window (Finkelstein and Sims, 2001). The standard deviation of this error tends to follow a consistent pattern across ecosystem types and increases linearly with the flux magnitude (Aubinet et al., 2012). Overall, random errors in NEE are difficult to quantify, but using simultaneous measurements from two collocated EC towers, they have been estimated at 15 % for a 30-minute interval (Eugster et al., 1997; Dragoni et al., 2007).

GPP and ER are commonly derived from NEE using flux-partitioning methods. The most established approach assumes that nighttime NEE consists solely of the ER component, since photosynthesis, and therefore GPP, is considered negligible in the absence of light (Reichstein et al., 2005; Aubinet et al., 2012). Nighttime ER is modeled using the Arrhenius equation, with air or soil temperature as the primary driver (Lloyd and Taylor, 1994). Air temperature is generally preferred because it better represents the landscape surrounding the EC tower, whereas soil temperature varies spatially and with depth across heterogeneous terrain (Helbig et al., 2017a, b). Daytime ER is then extrapolated to isolate the GPP contribution from the NEE measurements. Alternative approaches fit a light-response curve combined with a Q₁₀ equation to NEE measurements, accounting for the effects of photosynthetically active radiation (PAR) on GPP and air temperature on ER (Falge et al., 2001; Gilmanov et al., 2003; Lasslop et al., 2010b; Runkle et al., 2013; Helbig et al., 2017a). GPP and ER have greater uncertainties than tower measurements of NEE because they are modeled using additional data and rely on various assumptions (Lasslop et al., 2010a). In this study, we placed confidence in the flux-partitioning methods selected by the investigators at each EC tower. We therefore considered the resulting partitioned GPP and ER values to be credible representations of the underlying processes and suitable for use as reference data for model calibration and evaluation. EC NEE, GPP, and ER were averaged from 30-minute intervals to daily time steps, using at least 24 out of the theoretical 48 data points available per day. Hereafter, NEE_{EC}, GPP_{EC}, and ER_{EC} refer to the daily means of EC NEE, GPP, and ER.

All EC towers considered in this study are located in the tundra and taiga biomes, in areas underlain by sporadic, discontinuous, or continuous permafrost (Figure 1). Permafrost (ground that has remained frozen for more than 2 years) lies beneath an active layer that thaws during the growing season, enabling plant growth, as roots can only establish in thawed soil (Blume-Werry et al., 2019). Permafrost also restricts surface drainage, promoting water saturation and slowing decomposition rates (Wania et al., 2009; Robinson and Moore, 2000; Rouse et al., 1997; Maltby and Immirzi, 1993). These conditions can favor



the formation of wetlands, including peatlands as well as other seasonally or permanently waterlogged ecosystems, across both tundra and taiga biomes (Treat et al., 2022). Based on site descriptions, EC towers were grouped into three distinct ecosystem types (Table 1):

120 – **Taiga forests:** 7 EC towers are located in taiga forests, characterized by a vertically stratified vegetation structure, with an open canopy of coniferous trees and an understory of shrubs, mosses, and lichens (Crawford, 2013; Juday, 2025).

125 – **Upland tundra:** 5 EC towers are located in upland tundra, which may exhibit lower vegetation density and diversity, as well as reduced soil biological activity, compared with taiga forests (Crawford, 2013; Hagedorn et al., 2025). The landscape is treeless and dominated by dwarf shrubs, grasses, sedges, mosses, and lichens, as plant growth is constrained by cold temperatures, short growing seasons, and the shallow depth of the permafrost active layer (Crawford, 2013; Hu and Bliss, 2025; Juday, 2025; Péwé, 2025).

130 – **Wetlands:** 8 EC towers are located in wetlands, where the term “wetland” refers to a wide range of types, including peatlands, bogs, fens, marshes, wet meadows, and shrub swamps, present in both tundra and taiga biomes. Compared with taiga forests and upland tundra, wetlands may exhibit higher species richness (McPartland et al., 2019) and localized microtopography, such as hummocks and hollows, whose characteristics depend on water table depth (Rouse et al., 1997; Zhang et al., 2024).

3 L4C model

The L4C model provides global, daily estimates of NEE, GPP, and ER at 9-km resolution from March 31, 2015, to the present (Jones et al., 2017; Kimball et al., 2025). It takes as inputs

135 – A static global plant functional type (PFT) classification at 500-m resolution, retrieved from the Moderate Resolution Imaging Spectroradiometer (MODIS) MCD12Q1 Type 5 product (Friedl and Sulla-Menashe, 2019).

– Eight-day fraction of photosynthetically active radiation (canopy-intercepted FPAR) and leaf area index (LAI) data at 500-m resolution, retrieved from the Visible Infrared Imaging Radiometer Suite (VIIRS) VNP15A2H product (Myneni and Knyazikhin, 2018).

140 – Daily means of three-hourly data at 9-km resolution, retrieved from the SMAP SPL4SMGP product version 8 (Reichle et al., 2025), including 10-cm deep soil temperature (ST_{10}), surface skin temperature, incident shortwave solar radiation (SW_{in}), surface soil moisture (SSM), and rootzone soil moisture (RZSM). SSM and RZSM estimates are obtained by assimilating SMAP L-band brightness temperature observations into the Goddard Earth Observing System Version 5 Catchment Land Surface Model (GEOS-5 CLSM) (Reichle et al., 2019).

145 – Daily vapor pressure deficit (VPD) and minimum air temperature (MNT) at 0.25° (approximately 25-km resolution), retrieved from the GEOS-5 Forward Processing (FP) product (Lucchesi, 2018).



SW_{in} is combined with FPAR to compute canopy-absorbed photosynthetically active radiation (APAR), assuming that PAR constitutes 45 % of SW_{in} , as follows:

$$APAR = 0.45 \cdot SW_{in} \cdot FPAR = PAR \cdot FPAR \quad (2)$$

150 RZSM is rescaled using a normalized logarithmic transformation (Jones et al., 2017), and SSM is converted from volumetric units to relative wetness units. With the exception of APAR, the variables MNT, VPD, RZSM, ST, and SSM affect GPP and ER estimation only after being converted into stress scalars, denoted as S_{MNT} , S_{VPD} , S_{RZSM} , S_{ST} , and S_{SSM} . The derivation of these stress scalars is described later in Equations 7a-e.

The L4C model runs at a daily time step and is defined as follows:

$$155 \quad GPP(t) = \epsilon_{max} \cdot APAR(t) \cdot S_{MNT}(t) \cdot S_{VPD}(t) \cdot S_{RZSM}(t) \quad (3a)$$

$$ER(t) = AR(t) + HR(t) = \alpha \cdot GPP(t) + [k_1 \cdot SOC_1(t) + (1 - \eta) \cdot k_2 \cdot SOC_2(t) + k_3 \cdot SOC_3(t)] \cdot S_{ST}(t) \cdot S_{SSM}(t) \quad (3b)$$

GPP is modeled using a light-use efficiency approach (Jones et al., 2017; Xiao et al., 2013), where ϵ_{max} represents the bulk environmental reduction in PAR conversion efficiency. AR is modeled as a fixed proportion of GPP, determined by the coefficient α . HR is estimated using a cascading three-pool SOC decomposition model (Ise and Moorcroft, 2006; Kimball et al., 2008; 160 Jones et al., 2017), assuming that carbon fixed from atmospheric CO₂ through GPP enters the SOC pools as litterfall (L_{fall}). The daily SOC change for each of the three SOC pools is specified as:

$$SOC_1(t) = SOC_1(t-1) + [\lambda \cdot L_{fall}(t) - k_l \cdot SOC_1(t-1) \cdot S_{ST}(t) \cdot S_{SSM}(t)] \cdot dt \quad (4a)$$

$$SOC_2(t) = SOC_2(t-1) + [(1 - \lambda) \cdot L_{fall}(t) - k_s \cdot SOC_2(t-1) \cdot S_{ST}(t) \cdot S_{SSM}(t)] \cdot dt \quad (4b)$$

$$SOC_3(t) = SOC_3(t-1) + [\eta \cdot k_s \cdot SOC_2(t) \cdot S_{ST}(t) \cdot S_{SSM}(t) - k_r \cdot SOC_3(t-1) \cdot S_{ST}(t) \cdot S_{SSM}(t)] \cdot dt \quad (4c)$$

165 SOC_1 , SOC_2 , and SOC_3 represent the labile, structural, and recalcitrant SOC pools, respectively, with corresponding decay rates k_1 , $k_2 = 0.4 \cdot k_1$, and $k_3 = 0.01 \cdot k_1$. The model parameters λ and η account for the fraction of L_{fall} allocated to the SOC_1 and SOC_2 pools, and the fraction of material transferred from the SOC_2 pool to the SOC_3 pool, respectively. The parameters ϵ_{max} , k_l , λ , and η are treated as free parameters estimated during the optimization process. The model integration step dt is set to one day.

170 In the L4C model version 7, L_{fall} was derived as a constant daily fraction of the mean annual estimated net primary productivity (NPP), as follows:

$$L_{fall}(t) = \overline{NPP_{annual}} \cdot 1/365 = (1 - \alpha) \cdot \overline{GPP_{annual}} \cdot 1/365 \quad (5)$$

$\overline{NPP_{annual}}$ and $\overline{GPP_{annual}}$ denote the mean annual NPP and GPP, respectively, and the daily fraction is set to 1/366 for leap years. Instantaneous NPP is initially derived as $NPP(t) = GPP(t) - AR(t)$. In the L4C model version 8, the allocation timing 175 was changed from constant to dynamic, and is now determined using a leaf-loss function (L_{loss}), derived from climatological



LAI, as follows:

$$L_{\text{fall}}(t) = \overline{\text{NPP}_{\text{annual}}} \cdot [f_E \cdot dt + (1 - f_E) \cdot \frac{L_{\text{loss}}(t)}{\sum L_{\text{loss}}(t)}] \quad \text{with} \quad f_E = \frac{\min(\text{LAI})}{\max(\text{LAI})} \quad (6)$$

Here, f_E represents the proportion of the canopy that is evergreen. L_{loss} is computed using a triangular moving average centered on the current time step, where weights increase linearly toward the center. It represents the difference between lagged and leading climatological LAI values (Endsley et al., 2022).

In equations 3a-b and 4a-c, the stress scalars S_{MNT} , S_{VPD} , S_{RZSM} , S_{ST} , and S_{SSM} represent the ecosystem responses to their respective environmental variables and are defined as follows:

$$S_{\text{MNT}}(t) = \min(1, \max(0, \frac{\text{MNT}(t) - \text{MNT}_{\min}}{\text{MNT}_{\max} - \text{MNT}_{\min}})) \quad (7a)$$

$$S_{\text{VPD}}(t) = \min(1, \max(0, 1 - \frac{\text{VPD}(t) - \text{VPD}_{\min}}{\text{VPD}_{\max} - \text{VPD}_{\min}})) \quad (7b)$$

$$S_{\text{RZSM}}(t) = \min(1, \max(0, \frac{\text{RZSM}(t) - \text{RZSM}_{\min}}{\text{RZSM}_{\max} - \text{RZSM}_{\min}})) \quad (7c)$$

$$S_{\text{SSM}}(t) = \min(1, \max(0, \frac{\text{SSM}(t) - \text{SSM}_{\min}}{\text{SSM}_{\max} - \text{SSM}_{\min}})) \quad (7d)$$

$$S_{\text{ST}}(t) = \min(1, \exp(\beta_0 \cdot (\frac{1}{\beta_1} - \frac{1}{\text{ST}(t) - \beta_2}))) \quad (7e)$$

Each stress scalar ranges from 0 to 1, where a value of 0 indicates that the environmental variable fully constrains model estimates, while a value of 1 indicates no constraint. The thresholds MNT_{\min} , MNT_{\max} , VPD_{\min} , VPD_{\max} , RZSM_{\min} , RZSM_{\max} , SSM_{\min} , and SSM_{\max} are free parameters estimated during the optimization process. These are used as model thresholds and do not correspond to the actual minimum or maximum values within the time series. Similarly, β_0 is a free parameter, while β_1 and β_2 are fixed at 66.02 K and 227.13 K, respectively (Kimball et al., 2025). The behavior of the ecosystem response functions is shown in Figure A1.A1-C1. The GPP formulation originally includes a stress scalar based on the freeze-thaw state, computed using surface skin temperature from the SMAP SPL4SMGP product (Jones et al., 2017; Kimball et al., 2025).

However, it is not shown here, as this study focuses on the growing season.

L4C model estimates are initially derived at a 1-km sub-grid resolution for up to 8 MODIS MCD12Q1 PFT classes, and then averaged to 9-km resolution. In this study, only the L4C model estimates corresponding to the PFT class in which the EC towers are located were considered (Table 1). A total of two towers are located in the grassland (GRA) class, 8 in the shrubland (SHR) class, and 10 in the evergreen needleleaf forest (ENF) class. Hereafter, NEE_{L4C} , GPP_{L4C} , and ER_{L4C} refer to daily estimates derived from the L4C model, which were retrieved from the SMAP SPL4CMDL product version 8.



4 Method

4.1 Arctic-Subarctic adapted model formulations

In this study, we explored alternative GPP and ER model formulations that retain the core GPP and ER equations of the original L4C model version 8. We aimed to preserve the structure and variable set of the original L4C model while enabling the incorporation of constraints or additional flexibility guided by literature-based findings on ecosystem responses and flux-partitioning methods. Five different formulations are presented for both GPP and ER, with each formulation building incrementally on the previous one by incorporating earlier modifications along with additional adjustments. Testing modifications incrementally, rather than independently, allowed us to determine whether their interactions improved or degraded model performance.

The GPP formulations, labeled GPP₁ through GPP₅, mainly adjust ecosystem responses to environmental variables and are defined as follows (Table 3):

- GPP₁: Under sub-freezing air temperatures, photosynthetic activity is expected to be severely reduced, approaching cessation (Schaefer et al., 2012; Ensminger et al., 2004; Bowling et al., 2018; Parazoo et al., 2018). This behavior is not well represented in the original L4C model, where S_{MNT} still remains near 0.5 at 270 K (Figures 2, 3, 4.A2), indicating that GPP capacity is reduced by only half at this temperature. In the proposed formulation, GPP is ensured to cease when MNT is equal to or below 273.15 K by fixing the minimum threshold (MNT_{min}) of S_{MNT} to 273.15 K (Equation 7a).
- GPP₂ (defined as GPP₁ with additional adjustments): Some flux-partitioning methods use a nonlinear light-response curve to partition NEE_{EC} into GPP_{EC} and ER_{EC} (Lasslop et al., 2010b; Runkle et al., 2013), capturing the saturation of leaf-level photosynthesis at high solar irradiance. In the original L4C model, APAR directly scales the dynamic range of GPP and is not transformed through a transfer function into a stress scalar, as is the case for the other environmental variables (Equation 3a). In GPP₂, this linear dependence is replaced by a nonlinear stress scalar, S_{APAR}, inspired by the light-response curve, which is defined as follows:

$$GPP(t) = GPP_{max} \cdot S_{APAR}(t) \cdot S_{MNT}(t) \cdot S_{VPD}(t) \cdot S_{RZSM}(t) \quad (8a)$$

$$S_{APAR}(t) = \frac{APAR(t)}{APAR(t) + APAR_{crit}} \quad (8b)$$

At low APAR, GPP increases rapidly, but as APAR increases, the rate of increase slows down, and GPP asymptotically approaches a maximum value, GPP_{max}. This behavior is shown in Figure A1.D1. GPP_{max} and APAR_{crit} are free parameters estimated during the optimization process.

- GPP₃ (defined as GPP₂ with additional adjustments): In the original L4C model, GPP responds linearly to MNT, VPD, and RZSM (Equations 7a,b,c). In GPP₃, GPP responses to these variables are modeled with increased flexibility, with no assumed shape other than monotonicity, to allow varying rates of change across different ranges. To achieve this, they



230

are redefined as logistic ramp functions:

$$S_{MNT}(t) = \frac{g(MNT(t)) - g(MNT_{min})}{g(MNT_{max}) - g(MNT_{min})} \quad \text{with} \quad g(MNT(t)) = \frac{1}{1 + \exp(-\gamma_{MNT} \cdot (MNT(t) - MNT_{crit}))} \quad (9a)$$

$$S_{VPD}(t) = \frac{g(VPD(t)) - g(VPD_{min})}{g(VPD_{max}) - g(VPD_{min})} \quad \text{with} \quad g(VPD(t)) = \frac{1}{1 + \exp(\gamma_{VPD} \cdot (VPD(t) - VPD_{crit}))} \quad (9b)$$

$$S_{RZSM}(t) = \frac{g(RZSM(t)) - g(RZSM_{min})}{g(RZSM_{max}) - g(RZSM_{min})} \quad \text{with} \quad g(RZSM(t)) = \frac{1}{1 + \exp(-\gamma_{RZSM} \cdot (RZSM(t) - RZSM_{crit}))} \quad (9c)$$

235

In this formulation, the thresholds MNT_{min} , MNT_{max} , VPD_{min} , VPD_{max} , $RZSM_{min}$, and $RZSM_{max}$ are used to scale the stress scalars between 0 and 1, and are fixed to 273.15 K, 293.15 K, 0 kPa, 2.5 kPa, 0 $m^3 m^{-3}$, and 1 $m^3 m^{-3}$, respectively. The parameters MNT_{crit} , γ_{MNT} , VPD_{crit} , γ_{VPD} , $RZSM_{crit}$, and γ_{RZSM} are treated as free parameters and are estimated during the optimization process. The behavior of the logistic ramp functions is illustrated in Figure A1.A2-C2.

240

245

- GPP₄ (defined as GPP₃ with additional adjustments): Growing degree days (GDD) are widely used in agricultural and ecological studies as a proxy to plant development (Fotou Makouate and Zude-Sasse, 2025), and have recently been used to develop a phenology scheme that improved GPP modeling in a temperate bog (He et al., 2025). In the present formulation, GDD is incorporated into GPP modeling to capture the vegetation green-up and senescence phases through an additional stress scalar (S_{GDD}). GDD is first derived from mean air temperature using a base temperature of 273.15 K. It is then normalized for each site and each year using the annual minimum and maximum values, resulting in a normalized range from 0 to 1. This normalization ensures that GDD acts as a seasonal shape or trend driver, rather than a magnitude driver, which is instead represented by the instantaneous variables (APAR, MNT, VPD, and RZSM). Hereafter, GDD refers to normalized GDD and is used to derive S_{GDD} , as follows:

$$GPP_4(t) = GPP_{max} \cdot S_{APAR}(t) \cdot S_{MNT}(t) \cdot S_{VPD}(t) \cdot S_{RZSM}(t) \cdot S_{GDD}(t) \quad (10a)$$

$$S_{GDD}(t) = \frac{g(GDD(t))}{g\left(\frac{a}{a+b}\right)} \quad \text{with} \quad g(GDD(t)) = GDD(t)^a \cdot (1 - GDD(t))^b \quad (10b)$$

250

S_{GDD} is defined as a beta-like, bell-shaped function, normalized between 0 and 1 (Figure A1.D2). The parameters a and b are treated as free parameters and are estimated during the optimization process.

255

- GPP₅ (defined as GPP₄ with additional adjustments): Some studies have reported that water-saturated soil conditions limit oxygen and nutrient availability to plant roots, restrict cellular respiration, and consequently hinder photosynthetic activity (Kreuzwieser et al., 2004; Nawaz et al., 2025). Additionally, Peng et al. (2024) showed that the relationship between GPP and soil moisture may follow a bell-shaped curve at EC tower sites with PFTs similar to those in the present study (e.g., ENF, SHR, GRA; Table 1). A similar response has also been reported for peatlands (Valkenborg et al.,



2023). In GPP_5 , it is similarly assumed that GPP peaks at an optimal RZSM level, beyond which excessive moisture reduces efficiency. This assumption is tested by redefining S_{RZSM} as a beta-like, bell-shaped function, analogous to S_{GDD} (Equation 10b and Figure A1.D2):

$$S_{\text{RZSM}}(t) = \frac{g(\text{RZSM}(t))}{g\left(\frac{a}{a+b}\right)} \quad \text{with} \quad g(\text{RZSM}(t)) = \text{RZSM}(t)^a \cdot (1 - \text{RZSM}(t))^b \quad (11)$$

260 The parameters a and b are treated as free parameters and are estimated during the optimization process.

Regarding the ER modeling, we tested different formulations for the HR component while leaving the AR component unchanged. The ER formulations, labeled ER_1 through ER_5 , are described below (Table 3):

265

- ER_1 : Rather than using the L_{fall} estimation scheme from the baseline L4C model version 8, ER_1 instead adopts the one from version 7 (Equation 5). The L4C model transitioned from version 7 to version 8 over the course of the present study was conducted, during which the L_{fall} estimation scheme was modified. The version 7 scheme was retained to enable comparison with the one introduced in version 8. Additionally, HR response to SSM (S_{SSM}) is redefined as a logistic ramp, analogous to S_{RZSM} in GPP_3 (Equation 9c and Figure A1.A2). The original linear response (Equation 7d) was directly replaced because the logistic ramp can reproduce a linear behavior if the relationship between SSM and HR is actually linear. The ER response function to ST is unchanged but was recalibrated (Equation 7e).

270

- ER_2 (defined as ER_1 with additional adjustments): The L_{fall} estimation scheme is reverted to that of the baseline L4C model version 8.

275

- ER_3 (defined as ER_2 with additional adjustments): None of the established flux-partitioning methods requires SOC data to derive GPP and ER from NEE (Reichstein et al., 2005; Lasslop et al., 2010b; Runkle et al., 2013; Helbig et al., 2017a). Consequently, in ER_3 , we aimed to capture the added value of incorporating SOC dynamics in ER modeling. To this end, SOC dynamics are replaced by a single constant representing a baseline heterotrophic respiration rate, (R_{base}), as follows:

$$\text{ER}(t) = \alpha \cdot \text{GPP}(t) + R_{\text{base}} \cdot S_{\text{ST}}(t) \cdot S_{\text{SSM}}(t) \quad (12)$$

The parameter R_{base} is treated as a free parameter and is estimated during the optimization process.

280

- ER_4 (defined as ER_3 with additional adjustments): In the present formulation, we aimed to mimic the flux-partitioning methods that derive R_{base} every few days (Reichstein et al., 2005; Lasslop et al., 2010b; Runkle et al., 2013; Helbig et al., 2017a). R_{base} is then redefined as:

$$R_{\text{base}}(t) = (1 - \omega) \cdot R_{\text{base}}(t-1) + \omega \cdot R_0 \cdot \overline{S_{\text{ST}}(t) \cdot S_{\text{SSM}}(t)} \quad (13)$$

This follows a first-order auto-regressive (AR1) approach, in which the current value depends on the previous one and the 7-day backward mean of the product of temperature and moisture stress scalars ($\overline{S_{\text{ST}}(t) \cdot S_{\text{SSM}}(t)}$), weighted by the



285 parameter ω (ranging from 0 to 1). This approach introduces acclimation behavior by smoothing short-term variability in environmental conditions. The parameters R_0 and ω are treated as free parameters and are estimated during the optimization process.

– ER₅ (defined as ER₄ with additional adjustments): Endsley et al. (2022) showed that including an O₂ diffusion limitation in the HR response to SSM, which penalizes HR rates under high SSM conditions, improved seasonal ER performance.
290 In ER₅, we adopted the beta-like, bell-shaped function, analogous to S_{RZSM} in GPP₅ (Equation 11), to model HR response to SSM. This avoids to collect or estimate O₂ concentration data while still representing diminishing returns on HR under high SSM conditions.

In this study, daily VPD and MNT were retrieved from the Modern-Era Retrospective Analysis for Research and Applications, Version 2 (MERRA-2), M2T1NXSLV Version 5.12.4 product (Gelaro et al., 2017), instead of the GEOS-5 FP product,
295 because it is sparsely documented. MERRA-2 re-analysis dataset is better constrained by observations, exhibits a climatology comparable to GEOS-5 FP and is used in the L4C model calibration due to its longer period of record. Mean air temperature, required to derive GDD, was also retrieved from the MERRA-2 M2T1NXSLV product. Finally, RZSM and SSM from the SMAP SPL4SMGP product were retained in volumetric units (m³m⁻³), unlike in the original L4C model.

4.2 Growing season timing and data filtering

300 GPP_{EC} was used as an indicator to identify the growing season (Gonsamo et al., 2013). For each EC tower, GPP_{EC} values below the noise threshold of 0.05 gCm⁻²d⁻¹ were first attributed to the winter season and removed. Among the remaining values, those below the arbitrary threshold of the 10th percentile were considered part of the shoulder seasons (i.e., transitional periods between fully frozen and fully thawed states) and excluded, while values above the 99th percentile were treated as outliers and also removed. To ensure consistency in outlier detection, ER_{EC} values above the 99th percentile were similarly excluded.

305 Complementary filtering flags were applied to ensure biophysical plausibility of root-level soil activity and photosynthesis during the growing season from a modeling perspective. The specific criteria for these flags are as follows:

- ST_{10cm} \geq 275.15 K (i.e., 2 °C above freezing)
- ST_{20cm} \geq 275.15 K
- ST_{39cm} \geq 275.15 K (applied to ENF sites only, see Table 1)
- 310 – MNT \geq 275.15 K

ST_{20cm} and ST_{39cm} refer to soil temperature at 20 and 39 cm depths, respectively, and were retrieved from the SMAP SPL4SMGP product. For the remainder of this study, ST refers to ST_{10cm} as ST_{20cm} and ST_{39cm} are not used further.

After filtering, a total of 1,650 data points (23 %) remained for the upland tundra ecosystem, 4,632 data points (33 %) for the taiga forest ecosystem, and 3,653 data points (30 %) for the wetland ecosystem (Table 1).



315 4.3 Model formulation calibration

The AS-adapted GPP and ER formulations were calibrated separately for each ecosystem type (upland tundra, taiga forests, and wetlands), using GPP_{EC} and ER_{EC} as reference targets. The optimization framework for calibration used least-squares minimization via the MATLAB `lsqcurvefit` function (MathWorks, Inc., 2023), which minimizes the sum of squared differences between the model outputs and target values. This is an unconstrained optimization, with no additional penalty terms applied.

320 To mitigate overfitting, the optimization process was repeated 100 times using different random subsets, comprising 70 % of the data available for the ecosystem type (1,155 data points for upland tundra, 3,243 for taiga forests and 2,557 for wetlands). Final model parameter values were taken as the median across all runs. This approach aimed to capture diverse data combinations and promote a more stable and representative parameterization by smoothing out the influence of outliers or any individual biased subset. A 70 % subset size was arbitrarily chosen to balance between providing sufficient data for robust model calibration and

325 retaining enough data variability across the 100 iterations (Martinez Molera, 2025). Contrary to the global calibration of the original L4C model, no reference SOC data were used to constrain the recalibration over the AS environments. As a result, in ER_1 and ER_2 , only the SOC_1 pool was modeled to avoid potential parameter compensation and to prevent unrealistic SOC distribution across the original three pools. An initial guess was necessary for SOC_1 on March 31, 2015, to explicitly solve the SOC dynamics, since the system is formulated recursively and requires a starting value to iterate forward in time (Equation 4).

330 March 31, 2015, was chosen as the start of the simulation because it precedes the first date of the period of study. The initial guess was set to 0 $g\text{Cm}^{-2}$ for the first spin-up iteration, providing a neutral starting point to avoid biasing the early simulation. It was subsequently updated using the SOC value on March 31, 2022, corresponding to the last March 31 within the study period. A total of 20 spin-up iterations were performed.

4.4 Model formulation evaluation and validation

335 The AS-adapted GPP formulations were evaluated spatiotemporally, capturing the combined effects of spatial and temporal variability, using GPP_{EC} as the reference target. All available data points, including those used for calibration, were included in the evaluation. Model performance was quantified using three statistical metrics: the Pearson correlation coefficient (r), the unbiased root mean square error (ubRMSE), and bias (B). A rank was assigned to each formulation for each metric. The ranks were then averaged across the three metrics to obtain an overall score. This score was subsequently adjusted by a penalty factor

340 accounting for model complexity, as follows:

$$S_i = \left(\frac{1}{3} \sum_{j=1}^3 R_{ij} \right) \cdot P_i \quad \text{with} \quad P_i = \frac{n_i}{n_{\min}} \quad (14)$$

S_i is the final score of the i^{th} formulation, and R_{ij} is its rank for the j^{th} metric. The penalty factor of the i^{th} formulation, P_i , is determined by the number of free parameters (n_i ; Table 3) relative to the minimum numbers of free parameters across all formulations (n_{\min}). A lower score indicates better performance, whereas a higher score indicates worse performance. As a complement, temporal representativeness between formulations was assessed by computing the three metrics separately for each EC tower.



The AS-adapted ER formulations were evaluated and scored using the same approach as the GPP formulations, but with ER_{EC} as the reference target. Because ER modeling requires a GPP input (Equation 3), the GPP formulation with the lowest score was selected. Finally, the ER formulation with the lowest score, together with its corresponding GPP formulation, was 350 selected to derive AS-adapted estimates of NEE (NEE_{AS}). NEE_{AS} was then validated using NEE_{EC} as the reference target. This entire evaluation and scoring procedure was repeated independently for each ecosystem type.

5 Results

5.1 Gross primary production

This subsection presents the performance of the AS-adapted GPP formulations (GPP_1 through GPP_5) and GPP_{L4C} relative to 355 GPP_{EC} .

5.1.1 Upland tundra

Based on the spatiotemporal evaluation for upland tundra (Table 4), GPP_1 performs better than GPP_{L4C} in terms of B and ubRMSE (-0.32 vs. $0.41 \text{ gCm}^{-2}\text{d}^{-1}$ and 1.20 vs. $1.47 \text{ gCm}^{-2}\text{d}^{-1}$, respectively), although GPP_{L4C} achieves a higher r value (0.56 vs. 0.64). Introducing a nonlinear light-response in GPP_2 (Equation 8) leads to better performance compared with GPP_1 , 360 reducing B from -0.32 to $0.00 \text{ gCm}^{-2}\text{d}^{-1}$. In addition, ubRMSE decreases, and r increases, approaching the r observed for GPP_{L4C} . Replacing linear ramps with logistic ramps to simulate ecosystem responses in GPP_3 (Equation 9) increases model complexity but provides limited improvement over GPP_2 . GPP_4 incorporates GDD through an additional stress scalar 365 (Equation 10). This results in improved r and ubRMSE compared with GPP_3 (0.75 vs. 0.65 , and 0.84 vs. $0.96 \text{ gCm}^{-2}\text{d}^{-1}$, respectively). In GPP_5 , a bell-shaped function is used to simulate the influence of RZSM (Equation 11). This further improves r and ubRMSE, though B slightly increases (-0.02 vs. $-0.01 \text{ gCm}^{-2}\text{d}^{-1}$). After score computation, GPP_5 ranks first, followed by GPP_4 and GPP_3 (tied for second), and GPP_2 and GPP_1 in last place.

Across all formulations, $SVPD$ remains equal to 1 throughout the entire range of VPD variability (Figure 2.B3–F3). The use of a non linear light-response in GPP_2 introduces an early saturation (Figure 2.B6–F6), where modeled GPP peaks are lower than those of GPP_{EC} . This premature flattening is progressively reduced in GPP_4 and GPP_5 , due to the incorporation of GDD 370 and the use of a bell-shaped function for simulating RZSM influence.

Considering metrics across EC towers (Figure 8), GPP_4 and GPP_5 exhibit the highest median r (0.77 and 0.76) and the lowest median ubRMSE (0.65 and $0.71 \text{ gCm}^{-2}\text{d}^{-1}$). In contrast, GPP_5 , GPP_3 , and GPP_2 show the lowest median B with 0.04 , 0.05 , and $0.08 \text{ gCm}^{-2}\text{d}^{-1}$, respectively.

5.1.2 Taiga forests

375 The spatiotemporal evaluation for taiga forests (Table 4) indicates that GPP_1 performs better than GPP_{L4C} in terms of r (0.62 vs. 0.58) and ubRMSE (1.75 vs. $1.93 \text{ gCm}^{-2}\text{d}^{-1}$), although GPP_1 shows higher B (-0.43 vs. $-0.38 \text{ gCm}^{-2}\text{d}^{-1}$). As in up-



land tundra (Section 5.1.1), introducing a nonlinear light-response in GPP_2 (Equation 9) leads to overall better performance compared with GPP_1 , notably reducing B from $-0.43 \text{ gCm}^{-2}\text{d}^{-1}$ to $-0.07 \text{ gCm}^{-2}\text{d}^{-1}$. GPP_3 does not offer improvement over GPP_2 , aside from a slight reduction in B ($-0.02 \text{ gCm}^{-2}\text{d}^{-1}$ vs. $-0.07 \text{ gCm}^{-2}\text{d}^{-1}$). Due to the inclusion of GDD through an additional stress scalar (Equation 10), GPP_4 outperforms GPP_3 (0.74 vs. 0.67 for r , and 1.30 vs. 1.41 $\text{gCm}^{-2}\text{d}^{-1}$ for ubRMSE). Switching to a bell-shaped function for simulating RZSM influence in GPP_5 (Equation 11) does not result in improved performance compared with GPP_4 . After score computation, GPP_5 and GPP_4 are tied for first place, followed by GPP_3 and GPP_2 , with GPP_1 ranking last.

380 RZSM appears to be a negligible input in GPP_{L4C} , as S_{RZSM} remains equal to 1 throughout the entire range of RZSM variability (Figure 3.A4). However, RZSM gains more effect in GPP_1 through GPP_5 , although its effect remains weaker than that of MNT, VPD, and GDD (Figure 3.B4-F4). As in upland tundra (Section 5.1.1), the use of a nonlinear light-response in GPP_2 introduces an early saturation, underestimating GPP_{EC} peaks (Figure 3.B6–F6). However, this premature flattening persists in GPP_4 and GPP_5 , despite the incorporation of GDD and the use of a bell-shaped function for simulating RZSM influence.

390 Considering metrics across EC towers (Figure 8), the highest median r are obtained for GPP_4 and GPP_5 (0.79 and 0.76). These two formulations also achieve the lowest median ubRMSE, with $1.12 \text{ gCm}^{-2}\text{d}^{-1}$ for GPP_5 and $1.15 \text{ gCm}^{-2}\text{d}^{-1}$ for GPP_4 . GPP_3 and GPP_4 exhibits the lowest median B ($-0.14 \text{ gCm}^{-2}\text{d}^{-1}$).

5.1.3 Wetlands

395 Based on the spatiotemporal evaluation for wetlands (Table 4), GPP_1 outperforms GPP_{L4C} , notably exhibiting reduced ubRMSE and B (1.33 vs. $2.19 \text{ gCm}^{-2}\text{d}^{-1}$, and -0.40 vs. $1.31 \text{ gCm}^{-2}\text{d}^{-1}$, respectively). As seen in upland tundra and taiga forests (Sections 5.1.1 and 5.1.2), introducing a nonlinear light-response in GPP_2 (Equation 8) results in improved r (0.63 vs. 0.53), reduced ubRMSE (1.04 vs. $1.33 \text{ gCm}^{-2}\text{d}^{-1}$), and reduced B (-0.04 vs. $-0.40 \text{ gCm}^{-2}\text{d}^{-1}$), compared with GPP_1 . GPP_3 shows only a minor improvement over GPP_2 . Due to the inclusion of GDD through an additional stress scalar (Equation 10), GPP_4 outperforms GPP_3 (0.72 vs. 0.65 for r , and 0.92 vs. $1.01 \text{ gCm}^{-2}\text{d}^{-1}$ for ubRMSE). In contrast to upland tundra and taiga forests (Sections 5.1.1 and 5.1.2), using a bell-shaped function for simulating RZSM influence in GPP_5 (Equation 11), result in degraded performance compared with GPP_4 . Overall, GPP_4 ranks first, followed by GPP_3 , GPP_5 , and GPP_2 , with GPP_1 ranking last.

400 Similar to upland tundra (Section 5.1.1), S_{VPD} remains equal to 1 throughout the entire range of VPD variability across all formulations (Figure 4.B3–F3). Likewise, as observed in taiga forests (Section 5.1.2), RZSM appears to be a negligible input in GPP_{L4C} , with S_{RZSM} staying equal to 1 throughout the entire range of RZSM variability (Figure 4.A4). However, RZSM gains a considerable effect in GPP_1 through GPP_5 , especially under dry conditions (Figure 4.B4-F4). The introduction of the nonlinear light-response in GPP_2 triggers an early saturation (Figure 4.B6–F6), that persists throughout GPP_5 .

410 Across EC towers (Figure 8), GPP_4 and GPP_5 exhibit the highest median r (0.79 and 0.76). GPP_4 and GPP_3 exhibits the lowest median ubRMSE (0.76 and $0.79 \text{ gCm}^{-2}\text{d}^{-1}$, respectively), closely followed by GPP_5 ($0.82 \text{ gCm}^{-2}\text{d}^{-1}$) and GPP_3 ($0.86 \text{ gCm}^{-2}\text{d}^{-1}$). Median B is similar for GPP_2 through GPP_5 , with -0.21 , -0.22 , -0.23 , and $-0.19 \text{ gCm}^{-2}\text{d}^{-1}$, respectively.



5.2 Ecosystem respiration

This subsection presents the performance of the AS-adapted ER formulations (ER_1 through ER_5) and ER_{L4C} relative to ER_{EC} . As GPP_5 ranked first among the GPP formulations for upland tundra and taiga forests, it was used as the GPP input for the ER modeling. For wetlands, GPP_4 was used instead.

415 **5.2.1 Upland tundra**

Based on the spatiotemporal evaluation for upland tundra (Table 5), ER_1 , which uses the approach where mean annual NPP is allocated uniformly across the year to L_{fall} (Equation 5), performs better than ER_{L4C} . It exhibits higher r (0.51 vs. 0.43), reduced ubRMSE (0.72 vs. 0.99 $gCm^{-2}d^{-1}$), and reduced B (-0.09 vs. 0.38 $gCm^{-2}d^{-1}$). Switching to the dynamic allocation in ER_2 (Equation 6) leads to enhanced r (0.65), ubRMSE (0.60 $gCm^{-2}d^{-1}$), and B (-0.06 $gCm^{-2}d^{-1}$), compared with ER_1 .

420 Using a constant R_{base} term instead of a SOC model in ER_3 (Equation 12) results in r and ubRMSE close to those of ER_2 , and lower B (0.00 vs. -0.06 $gCm^{-2}d^{-1}$). Using a dynamic R_{base} in ER_4 (Equation 13) shows better performance than ER_3 , with greater r (0.73 vs. 0.61) and reduced ubRMSE (0.53 vs. 0.62 $gCm^{-2}d^{-1}$). In ER_5 , the use of a bell-shaped function to simulate SSM influence does not provide a clear benefit. After score computation, ER_4 ranks first, followed by ER_3 , ER_5 , and ER_2 , with ER_1 ranking last.

425 ST appears to have a stronger effect than SSM in ER_1 through ER_4 (Figure 5B1–E1 vs. B2–E2). S_{ST} mainly oscillates around 0.5, while S_{SSM} rapidly reaches 1 under dry conditions, and wet conditions do not constrain model outputs. In ER_5 , the use of a bell-shaped function to simulate SSM increases its effect (Figure 5F2), but without any improvement in performance, as previously observed.

430 Considering metrics across EC towers (Figure 8), the highest median r are obtained for ER_2 and ER_5 (0.67 and 0.62). The lowest median ubRMSE is observed for ER_5 ($0.41 gCm^{-2}d^{-1}$) and ER_4 ($0.42 gCm^{-2}d^{-1}$), closely followed by the other formulations. In terms of median B , ER_5 , ER_3 , and ER_4 show the smallest values with 0.01, -0.01, and $0.02 gCm^{-2}d^{-1}$.

5.2.2 Taiga forests

The spatiotemporal evaluation for taiga forests (Table 5) indicates that ER_1 outperforms ER_{L4C} , showing enhanced r (0.52 vs. 0.33), reduced ubRMSE (1.28 vs. $1.71 gCm^{-2}d^{-1}$), but slightly higher B (-0.15 vs. -0.11 $gCm^{-2}d^{-1}$). As in upland tundra (Section 5.2.1), switching from a constant to dynamic allocation of mean annual NPP to L_{fall} in ER_2 (Equation 6) results in enhanced performance over ER_1 . Using a constant R_{base} term instead of a SOC model in ER_3 (Equation 12) exhibits similar r (0.53 vs. 0.54) and ubRMSE (1.23 vs. $1.23 gCm^{-2}d^{-1}$), but lower B (-0.01 vs. -0.08 $gCm^{-2}d^{-1}$), compared with ER_2 . Using a dynamic R_{base} in ER_4 (Equation 13) shows better performance than ER_3 with greater r (0.59 vs. 0.53) and reduced ubRMSE (1.17 vs. $1.23 gCm^{-2}d^{-1}$). In ER_5 , the use of a bell-shaped function to simulate SSM influence does not provide any benefits.

440 After score computation, ER_4 ranks first, followed by ER_5 , ER_3 , and ER_2 , with ER_1 ranking last.



SSM appears to be a negligible input in ER_{L4C} , as S_{SSM} remains equal to 1 throughout the entire range of SSM variability (Figure 6.A2). However, SSM gains more effect in ER_1 through ER_5 , although its effect remains weaker than that of ST (Figure 6.B2-F2).

Across EC towers (Figure 8), median r is similar across formulations, ranging from 0.61 to 0.64. The same pattern is observed 445 for median ubRMSE, which ranges from 0.95 to $1.01 \text{ gCm}^{-2}\text{d}^{-1}$. The lowest median B are obtained for ER_3 and ER_2 , with 0.00 and $-0.02 \text{ gCm}^{-2}\text{d}^{-1}$, respectively.

5.2.3 Wetlands

Based on the spatiotemporal evaluation for wetlands (Table 5), ER_1 outperforms ER_{L4C} , exhibiting enhanced r (0.49 vs. 0.23), reduced ubRMSE (0.81 vs. $1.81 \text{ gCm}^{-2}\text{d}^{-1}$), and reduced B (-0.06 vs. $1.76 \text{ gCm}^{-2}\text{d}^{-1}$). Switching from a constant to 450 dynamic allocation of mean annual NPP to L_{fall} in ER_2 (Equation 6) slightly increases r (0.53 vs. 0.49), and reduces ubRMSE and B (0.78 vs. $0.81 \text{ gCm}^{-2}\text{d}^{-1}$, -0.02 vs. $-0.06 \text{ gCm}^{-2}\text{d}^{-1}$, respectively). Using a constant or dynamic R_{base} term instead of a SOC model in ER_3 and in ER_4 (Equations 12 and 13) does not result in enhanced performance. In ER_5 , the use of a bell-shaped function to simulate SSM influence does not provide any benefits either. After score computation, ER_3 and ER_2 are tied for first place, followed by ER_4 and ER_5 , with ER_1 ranking last.

455 As observed in taiga forests (Section 5.2.2), SSM appears to be a negligible input in ER_{L4C} , with S_{SSM} staying equal to 1 throughout the entire range of SSM variability (Figure 7.A2). However, SSM gains a considerable effect in ER_1 through ER_5 , especially under dry conditions (Figure 7.B2-F2). ER_{L4C} may overestimate ER_{EC} by up to a factor of two or three (Figure 7.A3). This magnitude discrepancy is largely removed in ER_1 through ER_5 , but a pattern persists, in which ER_{EC} are systematically overestimated at low values (approximately 0 to $1 \text{ gCm}^{-2}\text{d}^{-1}$) across all formulations (Figure 7.B3-F3).

460 Considering metrics across EC towers (Figure 8), median r is similar across formulations, ranging from 0.63 to 0.67. The same pattern is observed for median ubRMSE, with the highest value assigned to ER_1 ($0.58 \text{ gCm}^{-2}\text{d}^{-1}$) and the lowest to ER_4 ($0.48 \text{ gCm}^{-2}\text{d}^{-1}$). ER_1 and ER_2 exhibiting the lowest median B, with -0.01 and $-0.04 \text{ gCm}^{-2}\text{d}^{-1}$, respectively.

5.3 Net ecosystem CO₂ exchange

Using the scores assigned to the AS-adapted GPP and ER formulations (Sections 5.1 and 5.2), NEE_{AS} was derived differently 465 for each ecosystem type. For upland tundra and taiga forests, $NEE_{AS} = ER_4 - GPP_5$, while for wetlands $NEE_{AS} = ER_3 - GPP_4$.

Based on the spatiotemporal validation for upland tundra (Table 6), NEE_{AS} exhibits enhanced r (0.64 vs. 0.55), reduced ubRMSE (0.73 vs. $0.86 \text{ gCm}^{-2}\text{d}^{-1}$), and similar B (0.01 vs. $-0.03 \text{ gCm}^{-2}\text{d}^{-1}$), compared with NEE_{L4C} . This improvement is also observed when considering the median r and ubRMSE across all EC towers (0.62 vs. 0.44 for r , 0.69 vs. $0.90 \text{ gCm}^{-2}\text{d}^{-1}$ for ubRMSE). However, median B changed from 0.06 to $-0.12 \text{ gCm}^{-2}\text{d}^{-1}$.

470 For taiga forests, the spatiotemporal validation indicates (Table 6) that NEE_{AS} outperforms NEE_{L4C} (0.63 vs. 0.55 for r , 1.09 vs. $1.17 \text{ gCm}^{-2}\text{d}^{-1}$ for ubRMSE, and 0.02 vs. $0.26 \text{ gCm}^{-2}\text{d}^{-1}$ for B). Across EC towers, the same pattern is observed: median ubRMSE and B are reduced (0.97 vs. $1.04 \text{ gCm}^{-2}\text{d}^{-1}$ and -0.09 vs. $0.40 \text{ gCm}^{-2}\text{d}^{-1}$, respectively), median r is higher (0.60 vs. 0.54).



Finally, for wetlands, the spatiotemporal validation indicates (Table 6) that NEE_{AS} exhibits reduced ubRMSE and B (0.93
475 vs. $0.99 \text{ gCm}^{-2} \text{d}^{-1}$ and 0.01 vs. $0.45 \text{ gCm}^{-2} \text{d}^{-1}$, respectively), but similar r (0.48 vs. 0.47), compared with NEE_{L4C} . Improvement is also observed when considering the median B across all EC towers (0.22 vs. $0.73 \text{ gCm}^{-2} \text{d}^{-1}$), but the median ubRMSE is similar (0.82 vs. $0.79 \text{ gCm}^{-2} \text{d}^{-1}$), and the median r is lower (0.33 vs. 0.50).

6 Discussion

This section discusses how the modifications implemented in the AS-Adapted GPP and ER model formulations affected their
480 performance relative to GPP_{EC} and ER_{EC} . We specifically identify candidate GPP model adjustments for operational implementation, evaluate the contribution of incorporating SOC dynamics into ER modeling, examine the influence of input variables, and highlight the limitations of our study.

6.1 Candidate GPP model adjustments

Implementing a nonlinear light-response function to represent the influence of APAR on GPP (GPP_2 , Equation 8) appears
485 to be the most effective adjustment tested for reducing both ubRMSE and B across the three ecosystem types (Section 5.1, and Table 4, Figure 8). However, our results indicate that this adjustment requires careful parametrization, as it can lead to underestimation of GPP peaks (Figures 2–4).

Adding GDD into the GPP modeling (Equation 10) complements the nonlinear light-response adjustment by further reducing ubRMSE and predominantly improving r across the three ecosystem types (Section 5.1, Table 4, Figure 8). These results
490 suggest that the current L4C model may lack a phenological proxy that accounts for the progressive functional adjustment of vegetation to environmental conditions over time (Maire et al., 2012), thereby complementing the instantaneous proxies currently used as inputs. Vegetation indices are assumed to capture vegetation phenology by tracking seasonal changes in canopy structure and greenness. Because GDD is derived from air temperature and MNT is used as a proxy for the instantaneous temperature response of GPP, replacing GDD with a vegetation index may help reduce redundancy (Huang et al., 2019; Pulliainen
495 et al., 2024). In this context, LAI or normalized difference vegetation index (NDVI) could potentially serve this role. However, LAI is likely to introduce additional redundancy, as VIIRS LAI retrievals are already used to derive FPAR, which represents canopy phenology in the GPP formulation (Equation 2). In contrast, NDVI may provide a more independent phenological proxy without duplicating existing model inputs. Nonetheless, MODIS and VIIRS vegetation indices exhibit large uncertainties at high northern latitudes, particularly during shoulder seasons, due to extensive cloud cover and snow contamination (Xu
500 et al., 2018; Pu et al., 2023).

Overall, the nonlinear light-response adjustment appears to be the strongest candidate for correcting GPP magnitude discrepancies, while incorporating GDD emerges as the most effective adjustment to improve GPP seasonal dynamics. These two findings are consistent with McCallum et al. (2013), where the authors reported that the inclusion of temperature acclimation and nonlinear light-response in GPP modeling in Russian boreal forests improved model performance. Future studies could
505 explore more complex light-response functions, such as a rectangular hyperbolic function, where the parameters may vary



temporally with temperature, as suggested by Wang et al. (2014a). However, testing this approach would imply departing from the current multiplicative structure of the L4C model, in which direct mechanistic forcing–response behaviors are represented. Prior work also suggests that vegetation green-up onset is influenced by winter chilling accumulation and precipitation (Fu et al., 2014). Greater accumulation of chilling days may lead to earlier green-up, as vegetation exposed to colder winter temperatures requires less thermal accumulation (less GDDs) to initiate spring growth. In contrast, higher winter precipitation may contribute to delayed green-up through thicker snowpacks, cooler soil temperatures, and increased cloud cover that reduces incoming radiation. Future improvements could therefore integrate winter chilling days and precipitation into the normalized GDD-based phenological proxy to better represent early-season GPP dynamics.

6.2 Comparison of SOC-based and empirical approaches for ER modeling

515 Updating the allocation of mean annual NPP to L_{fall} from a constant to a LAI-based formulation to represent SOC dynamics (ER₁ vs. ER₂; Equations 5 and 6) improves ER model performance. Both the spatiotemporal evaluation and the median metrics across EC towers indicate higher r and lower ubRMSE and B, with stronger improvements for upland tundra and weaker improvements for taiga forests and wetlands (Table 5 and Figure 8). The benefits are limited relative to the added model complexity, especially in taiga forests and wetlands, compared with the simpler approach that replaces SOC dynamics 520 with a single constant R_{base} (ER₃, Equation 12). Based on the spatiotemporal evaluation, introducing temporal variability in R_{base} (ER₄, Equation 13) leads to improved performance in upland tundra and taiga forests (Table 5). However, the median metrics across EC towers do not indicate a clear improvement across the three ecosystems (Figure 8).

Overall, using SOC dynamics with the L_{fall} estimation scheme from the L4C model version 8 to model ER appears to be the most suitable approach, as it outperforms version 7 and is physically grounded and mechanistically interpretable compared 525 with the two empirical approaches. Continuing to explore alternative ways to estimate L_{fall} may be a promising direction for future research. However, the assumption that mean annual NPP can serve as a proxy for the magnitude of L_{fall} may not be realistic (Sierra et al., 2022). In addition, the timing of NPP allocation to L_{fall} may not accurately reflect actual changes in aboveground biomass, particularly given the large uncertainties in LAI and FPAR retrievals at high northern latitudes (Xu et al., 2018; Pu et al., 2023). Furthermore, because NPP is derived from modeled GPP, any inaccuracies in GPP propagate 530 directly into modeled L_{fall} , SOC, and ultimately ER. Finally, recent work in Alaska has shown that implementing vertical SOC transport to simulate depth-dependent L_{fall} , SOC distribution, and corresponding HR rates may further improve ER estimates (Yi et al., 2020).

6.3 Tested but unretained GPP and ER model adjustments

Implementing logistic ramps to represent GPP responses to MNT, VPD, and RZSM stress (GPP₃, Equation 9) provides limited 535 benefits based on the spatiotemporal evaluation (GPP₂ vs. GPP₃ in Table 4). However, this adjustment appears to improve median r and ubRMSE across EC towers (GPP₂ vs. GPP₃ in Figure 8.A1-C1). This suggests that MNT, VPD, and RZSM may exhibit nonlinear interactions with GPP, but the added value may not justify the increased complexity required to implement this adjustment.



The spatiotemporal evaluation indicates that using a bell-shaped function to represent RZSM influence on GPP (GPP₅, 540 Equation 11) provides only a limited performance improvement in upland tundra and no improvement in taiga forests (Table 4). One possible explanation is that, in upland tundra, RZSM exhibits both dry and wet conditions across years and EC tower sites (grey histogram in Figure 2.F4), whereas in taiga forests, conditions remain mostly dry with less seasonal variation (Figure 3.F4). This pattern is supported by the bimodal distribution of RZSM in upland tundra, in contrast to the unimodal distribution in taiga forests. Nevertheless, the RZSM distribution in wetlands is bimodal (Figure 4.F4), with both dry and wet 545 conditions, but the bell-shaped function worsens the performance of modeled GPP (Table 4). The diminishing returns under wet conditions appear to penalize model calibration, indicating a different ecosystem response to RZSM in wetlands compared with upland tundra and taiga forests. This may reflect the adaptation of wetland vegetation to anaerobic conditions, where excessive RZSM does not hinder photosynthesis activity. Although several studies show that wetlands and peatlands are more 550 sensitive to drought than to flooding (Churchill et al., 2015; Olefeldt et al., 2017; Heinzelmann et al., 2025), clear evidence is lacking to suggest that GPP in wetlands does not exhibit diminishing returns under high RZSM conditions. It is also noteworthy 555 that the bell-shaped function does not improve model performance for any ecosystem when normalized RZSM is used (not shown), as is the case in the original L4C model (Section 3). The bell-shaped function offers no clear benefit neither when considering median metrics across EC towers (Figure 8). Finally, the L4C model methodology focuses on direct mechanistic forcing-response behavior, where instantaneous RZSM data are used as input. However, a temporal lag in GPP response to 560 RZSM saturation may be expected, as it can take several days to weeks for soil oxygen levels to become depleted to the point of restricting aerobic processes under saturation. A larger number of EC towers should also be included to increase RZSM variability during calibration before drawing conclusions about the value of this adjustment for North American AS regions.

As in the GPP modeling, the use of a bell-shaped function to represent SSM influence on ER provides no clear improvement, 565 regardless of ecosystem type or whether dry and wet SSM conditions are included during calibration (Table 5 and Figures 5-8). These results indicate that an unidirectional function ramp is more appropriate, with dry conditions limiting ER rates, and no diminishing returns under wet conditions. The same conclusion is drawn when SSM expressed in relative wetness units is used (not shown), as in the original L4C model (Section 3). This finding partly contrasts with Endsley et al. (2022), who reported 570 improved seasonal ER performance after adding an O₂ diffusion limitation (also based on SSM) to the original monotonic linear response, thereby penalizing ER rates under high SSM. The differing behavior between studies may first be attributed to differences in SSM response functions. In addition, in our study the GPP formulation used as input to ER already incorporates 575 a bell-shaped response to RZSM for upland tundra and taiga forests, and in Endsley et al. (2022), the SPL4SMGP product did not yet account for peatland hydrology (Reichle et al., 2023).

6.4 Key drivers in shaping model performance

As VPD rises, indicating atmospheric dryness, plants typically show stomatal closure to minimize water loss, which in turn 570 reduces their photosynthetic activity (López et al., 2021). However, in upland tundra and wetlands, GPP appears insensitive to VPD as the corresponding stress scalar S_{VPD} remains equal to 1 across all five AS-adapted formulations (Figures 2.B3-F3 and 4.B3-F3). This suggests that either the VPD response is inadequately represented in the formulations, or that vegetation in



these areas is inherently less responsive to stomatal closure than in taiga forests, where S_{VPD} strongly constrains the modeling (Figure 3.B3-F3). Indeed, VPD distributions are similar across the three ecosystem types, which supports the idea that the
575 observed differences in S_{VPD} are not due to differing environmental conditions, but rather to ecosystem-specific sensitivity. In other words, for the same VPD values, the model applies a stronger constraint to vegetation photosynthetic activity in taiga forests, while in upland tundra and wetlands it remains unconstrained. These findings are consistent with those of Chen et al. (2023), where the authors observed that increasing VPD did not hinder vegetation growth in northern peatlands. Additionally, Zona et al. (2023) reported that VPD was not correlated to GPP at monthly scales in Arctic tundra, while Mirabel et al. (2023)
580 found that tree growth in the Canadian boreal forest responded negatively to rising VPD.

Across all three ecosystem types, the most notable model improvement arises from revising the influence of APAR and AT (through GDD) on GPP (Table 4, Figure 8, Section 6.1). Interestingly, APAR and AT are also the two drivers primarily used to partition NEE_{EC} into GPP_{EC} and ER_{EC} (Section 2). This indicates that model performance is inherently entangled with these two drivers, rather than to VPD, RZSM, SSM, SOC, or ST. It is important to note that drivers used in the L4C
585 model formulations are provided at 9-km and 25-km resolution (except FPAR), which is coarse relative to EC tower footprints (Sections 2 and 3). Some of the discrepancies between EC measurements and model estimates may therefore be attributed to representativeness errors, as the coarse model resolution is expected to smooth spatial variability that is captured by the EC measurements. Coupled with the candidate GPP model adjustments (Section 6.1), using higher spatial resolution PAR and AT inputs could represent a promising avenue for improving GPP estimates and, consequently, ER estimates in future studies.

590 6.5 Limitations

Although the best-scoring GPP and ER formulations showed performance gains relative to the original L4C model, particularly for GPP, the resulting improvement in NEE performance is more modest (Tables 4, 5, and Figure 8 compared with Table 6). These results suggest that developing more accurate representations of ER and GPP does not necessarily translate into improved
595 NEE_{AS} , thereby directly affecting its ability to accurately predict short-term transitions between CO_2 sink and source states.

Regardless of whether NEE_{EC} is partitioned into GPP_{EC} and ER_{EC} using daytime data, nighttime data, or a combination of both, daytime ER_{EC} is derived from a fitted Q_{10} (power-based) or Arrhenius (exponential-based) function (Section 2). These functions depend solely on temperature and estimate the combined contribution of AR and HR, treating both components as a single and inseparable flux. In the L4C model and the tested AS-adapted formulations, ER is explicitly represented as the
600 sum of AR and HR, with both components estimated separately using multiple drivers, including APAR, GDD, MNT, VPD, RZSM, ST, and SSM. This approach is based on the assumed linkages between GPP and AR, and between GPP, L_{fall} , SOC and HR (Kimball et al., 2008), resulting in a more mechanistic and interaction-rich framework than partitioning methods. Consequently, calibrating ER formulations is challenging, as the reference ER is obtained from partitioning using a simpler, empirical approach, which may limit model performance. If the ultimate goal is to estimate the CO_2 budget accurately rather
605 than to predict the underlying GPP and ER components, it may be advantageous to calibrate the L4C model using NEE_{EC} as the reference, rather than relying on GPP_{EC} and ER_{EC} as intermediate references. However, this approach prevents validating

whether the modeled GPP and ER truly reflect the underlying processes. For future research, it could also be valuable to partition NEE_{EC} into GPP_{EC} and ER_{EC} using a more mechanistic approach, similar to the L4C model, explicitly distinguishing between AR and HR.

610 Finally, several studies have shown that GPP responds to the ratio of leaf-internal to ambient CO₂ concentration (Wang et al., 2014b, 2017). Although this ratio is regulated by environmental conditions such as temperature and VPD, neither the original L4C model nor the tested formulations explicitly accounts for the response of GPP to changes in ambient CO₂ concentration. Because ambient CO₂ varies over time and may continue to increase in the future, this omission may limit the ability of the L4C model to accurately predict GPP over long temporal scales.

615 7 Conclusions

The goal of this study was to refine the integration of energy and moisture proxies into the SMAP L4C GPP and ER modeling for the North American AS growing season. Alternative GPP and ER model formulations were calibrated and evaluated against GPP_{EC} and ER_{EC} across upland tundra, taiga forests and wetlands, covering the period from 2015 to 2022. Ultimately, we recommend two key adjustments related to energy proxies to enhance the L4C model ability to monitor the GPP process:

620

- Implementing a nonlinear light-response, particularly to reduce ubRMSE and B;
- Incorporating GDD to reflect vegetation green-up and senescence phases, thereby improving seasonal dynamics.

In contrast, model adjustments related to moisture proxies (VPD, RZSM, SSM) for both ER and GPP modeling do not currently emerge as essential for future operational implementation. Moreover, evaluating the benefits of integrating SOC dynamics into ER modeling remains challenging, even though the L4C version 8 approach represents an improvement over that of version 7, 625 and therefore further research into ER modeling is recommended.

In addition, we encourage the scientific community to harmonize strategies between flux-partitioning methods and mechanistic modeling approaches (such as the L4C model), particularly for estimating ER and its underlying HR and AR components. The alignment between partitioning and modeling frameworks is essential to enhance the reliability of spatial extrapolation of GPP_{EC} and ER_{EC} using satellite-based TCF models.

630 While GPP and AR are dominant during the growing season, the winter and shoulder seasons also play a critical role in shaping the annual CO₂ budget (Kim et al., 2013; Natali et al., 2019), because HR becomes the primary contributor when GPP and AR are minimal or absent. Therefore, future studies will focus on adjusting GPP and ER modeling during these periods to provide improved year-round estimates of NEE, GPP, and ER, as well as more accurate annual CO₂ budgets for North-American AS environments.

635 *Author contributions.* RM, ArM, and AR designed and conducted the study, and wrote the first draft of the manuscript. KAE and JSK provided scientific support throughout the study and contributed to the second version of the manuscript. OS, HA, SNW, AM provided some of the eddy covariance data. All authors contributed to the final version of the manuscript.



Competing interests. The authors declare no conflict of interest.

Acknowledgements. R. Madelon, A. Mialon and A. Roy acknowledge fundings from the Université de Toulouse 3 Paul Sabatier in France, 640 and the Université du Québec à Trois-Rivières in Canada through the Universalis Causa, Samuel-de-Champlain, Programme d'Aide à L'Internationalisation de la Recherche (PAIR), Fonds Canadien de l'Innovation (FCI) and Conseil de Recherches en Sciences Naturelles et en Génie du Canada (CRSNG), and Fonds de recherche du Québec (FRQ) grants. J.S. Kimball and K.A. Endsley acknowledge fundings from NASA (grant no. NX14AI50G). G. De Lannoy acknowledges funding from KU Leuven C1 (C14/21/057). O. Sonnentag acknowledges financial support through the Canada Research Chair and NSERC Discovery Grants programs, ArcticNet, a Network of Centres of 645 Excellence Canada, the Canada First Research Excellence Fund's Global Water Futures program (Northern Water Futures), and the Polar Continental Shelf Program. This research made use of eddy covariance data from the AmeriFlux network (<https://ameriflux.lbl.gov>). Additional eddy covariance data were directly provided by the principal investigators O. Sonnentag and S. N. Williamson. We thank all the principal investigators and site teams of the eddy covariance tower sites (listed in Table 1) for their sustained efforts in site maintenance, data processing, and data sharing. The SMAP SPL4CMDL Version 8 product can be downloaded from the National Snow and Ice Data 650 Center (NSIDC) website at: <https://nsidc.org/data/SPL4CMDL/Versions/8>. The SMAP SPL4SMGP Version 8 product can be downloaded at: <https://nsidc.org/data/SPL4SMGP/Versions/8>. The MERRA-2 M2T1NXSLV Version 5.12.4 product is available at: goldsmr4.gesdisc.eosdis.nasa.gov/data/MERRA2/M2T1NXSLV.5.12.4.

All the authors thank the indigenous and northern communities for agreeing to the installation of eddy covariance towers on their territory. As a non-native English speaker, R. Madelon acknowledges the use of artificial intelligence tools to improve the writing quality of the manuscript.



Site name	Site ID	Coordinates	Years	Ecosystem	PFT	NDP	Reference
Iqaluktuutiaq Mesic	CA-IQm	69.08°N, -104.58°E	[2022, 2023[Upland Tundra	GRA	68	Madelon et al. (2025)
Iqaluktuutiaq Wetland	CA-IQw	69.08°N, -104.58°E	[2022, 2023[Wetland	GRA	22	Madelon et al. (2025)
Havikpak Creek	CA-HPC	68.32°N, -133.52°E	[2016, 2023[Taiga Forest	SHR	371	Sonnentag and Marsh (2021a)
Scotty Creek Bog	CA-SCB	61.31°N, -121.30°E	[2015, 2023[Wetland	ENF	633	Sonnentag and Quinton (2021)
Scotty Creek Landscape	CA-SCC	61.31°N, -121.30°E	[2015, 2023[Taiga Forest	ENF	733	Sonnentag and Quinton (2018)
Smith Creek	CA-SMC	63.15°N, -123.25°E	[2017, 2023[Taiga Forest	ENF	312	Sonnentag (2021)
Trail Valley Creek	CA-TVC	68.75°N, -133.50°E	[2015, 2023[Upland Tundra	SHR	620	Sonnentag and Marsh (2021b)
Bonanza Creek Black Spruce	US-BZS	64.70°N, -148.32°E	[2017, 2023[Taiga Forest	ENF	652	Euskirchen (2022d)
Bonanza Creek Old Thermokarst Bog	US-BZo	64.69°N, -148.33°E	[2018, 2023[Wetland	ENF	548	Euskirchen (2022c)
Bonanza Creek Rich Fen	US-BZF	64.70°N, -148.31°E	[2017, 2023[Wetland	ENF	689	Euskirchen (2022b)
Bonanza Creek Thermokarst Bog	US-BZB	64.70°N, -148.32°E	[2017, 2023[Wetland	ENF	680	Euskirchen (2022a)
Eight Mile Lake	US-EML	63.88°N, -149.25°E	[2015, 2021[Upland Tundra	SHR	571	Bracho et al. (2021)
Imnavait Creek Heath Tundra	US-ICh	68.61°N, -149.30°E	[2015, 2023[Upland Tundra	SHR	314	Euskirchen et al. (2022a)
Imnavait Creek Sedge Tundra	US-ICs	68.61°N, -149.31°E	[2015, 2023[Wetland	SHR	336	Euskirchen et al. (2022b)
Imnavait Creek Tussock Tundra	US-ICt	68.61°N, -149.30°E	[2021, 2023[Upland Tundra	SHR	77	Euskirchen et al. (2022c)
Poker Flats Black Spruce	US-Prr	65.12°N, -147.49°E	[2015, 2023[Taiga Forest	ENF	827	Iwahana et al. (2023)
Poker Flats Fire Scar	US-Rpf	65.12°N, -147.43°E	[2015, 2023[Taiga Forest	ENF	852	Ueyama et al. (2023b)
University Of Fairbanks	US-Uaf	64.87°N, -147.86°E	[2015, 2023[Taiga Forest	ENF	885	Ueyama et al. (2023a)
Yukon-Kuskokwim Delta Burned	US-YK1	61.27°N, -163.22°E	[2019, 2023[Wetland	SHR	330	Natali (2024)
Yukon-Kuskokwim Delta Unburned	US-YK2	61.26°N, -163.26°E	[2019, 2023[Wetland	SHR	415	Natali (2025)

Table 1. List of the 20 eddy covariance (EC) tower sites used in this study. Ecosystem types were assigned based on site descriptions while plant functional type (PFT) classes were assigned using the Moderate Resolution Imaging Spectroradiometer (MODIS) MCD12Q1 type 5 product (Friedl and Sulla-Menashe, 2019). GRA, SHR, and ENF stand for grassland, shrubland, and evergreen needleleaf forest, respectively. Column 7 shows the number of data points (NDP) within the EC net ecosystem CO₂ exchange (NEE_{EC}), gross primary production (GPP_{EC}), and ecosystem respiration (ER_{EC}) time series after daily averaging and data filtering (see Sections 2 and 4.2).



Abbreviation	Definition
AS	Arctic-Subarctic
L4C model	Soil Moisture Active Passive Level-4 Terrestrial Carbon Flux model
EC	Eddy covariance
PFT	Plant functional type
NEE	Net ecosystem CO ₂ exchange [gCm ⁻² d ⁻¹]
GPP	Gross primary production [gCm ⁻² d ⁻¹]
ER	Ecosystem respiration [gCm ⁻² d ⁻¹]
AR	Autotrophic respiration [gCm ⁻² d ⁻¹]
HR	Heterotrophic respiration [gCm ⁻² d ⁻¹]
NPP	Net primary production [gCm ⁻² d ⁻¹]
PAR	Photosynthetically active radiation [MJm ⁻² d ⁻¹]
FPAR	Canopy-intercepted fraction of absorbed photosynthetically active radiation [dim.]
APAR	Canopy-absorbed photosynthetically active radiation [MJm ⁻² d ⁻¹]
MNT	Minimum air temperature [K]
VPD	Vapor pressure deficit [kPa]
RZSM	Rootzone soil moisture [m ³ m ⁻³]
SSM	Surface soil moisture [m ³ m ⁻³]
ST	Soil temperature [K]
SOC	Soil organic carbon [gCm ⁻²]
L _{fall}	Litterfall [gCm ⁻²]
GDD	Normalized growing degree days [dim.]
S _x	Stress scalar corresponding to the environmental variable x [dim.]
LAI	Leaf area index [dim.]
NDVI	Normalized difference vegetation index [dim.]

Table 2. Summary of frequently used abbreviations.



AS-adapted formulation	Free parameters	Model specificity
GPP ₁	ϵ_{\max} , MNT _{max} , VPD _{min} , VPD _{max} , RZSM _{min} , RZSM _{max}	MNT _{min} is set to 273.15 K
GPP ₂	GPP _{max} , APAR _{crit} , MNT _{max} , VPD _{min} , VPD _{max} , RZSM _{min} , RZSM _{max}	Nonlinear light response to APAR
GPP ₃	GPP _{max} , APAR _{crit} , γ_{MNT} , γ_{VPD} , VPD _{crit} , γ_{RZSM} , RZSM _{crit}	Nonlinear responses to MNT, VPD and RZSM
GPP ₄	GPP _{max} , APAR _{crit} , γ_{MNT} , γ_{VPD} , VPD _{crit} , γ_{RZSM} , RZSM _{crit} , a _{GDD} , b _{GDD}	Incorporation of GDD
GPP ₅	GPP _{max} , APAR _{crit} , γ_{MNT} , γ_{VPD} , VPD _{crit} , a _{RZSM} , b _{RZSM} , a _{GDD} , b _{GDD}	Bell-shaped response to RZSM
ER ₁	α , k ₁ , λ , β_0 , γ_{SSM} , SSM _{crit}	Constant daily allocation of annual mean NPP to L _{fall}
ER ₂	α , k ₁ , λ , β_0 , γ_{SSM} , SSM _{crit}	Dynamic daily allocation of annual mean NPP to L _{fall}
ER ₃	α , R _{base} , β_0 , γ_{SSM} , SSM _{crit}	Constant R _{base} instead of SOC dynamic
ER ₄	α , R ₀ , ω , β_0 , γ_{SSM} , SSM _{crit}	Dynamic R _{base} (t)
ER ₅	α , R ₀ , ω , β_0 , a _{SSM} , b _{SSM}	Bell-shaped response to SSM

Table 3. Summary of the specificity of each Arctic-Subarctic (AS) adapted model formulation of the L4C model. Column 1 lists the gross primary production (GPP) and ecosystem respiration (ER) formulations, labeled GPP₁ through GPP₅ and ER₁ through ER₅, respectively. The free parameters estimated during the optimization process are provided in column 2. Each GPP and ER formulation is incrementally built on the previous one by incorporating its modifications along with an additional change summarized in column 3. APAR, MNT, VPD, RZSM, SSM, GDD, NPP, L_{fall}, SOC, R_{base}, denote absorbed photosynthetically active radiation, minimum air temperature, vapor pressure deficit, rootzone soil moisture, surface soil moisture, normalized growing degree days, net primary productivity, litterfall, soil organic carbon, and baseline heterotrophic respiration, respectively. Refer to Sections 3 and 4.1 for a description of each model formulation and parameter.



GPP	Upland Tundra			Taiga Forests			Wetlands		
	r	ubRMSE	B	r	ubRMSE	B	r	ubRMSE	B
GPP _{L4C}	0.64	1.47	0.41	0.58	1.93	-0.38	0.48	2.19	1.31
GPP ₁	0.56	1.20	-0.32	0.62	1.75	-0.43	0.53	1.33	-0.40
GPP ₂	0.62	0.99	0.00	0.67	1.43	-0.07	0.63	1.04	-0.04
GPP ₃	0.65	0.96	-0.01	0.67	1.41	-0.02	0.65	1.01	-0.00
GPP ₄	0.75	0.84	-0.01	0.74	1.30	-0.00	0.72	0.92	0.00
GPP ₅	0.77	0.80	-0.02	0.74	1.29	-0.02	0.67	0.99	-0.05

Table 4. Spatiotemporal performance of modeled **gross primary production (GPP)** against daily-averaged eddy covariance GPP (GPP_{EC}) in upland tundra, taiga forests, and wetlands during the growing season. GPP_{L4C} refers to GPP from the original L4C model, while GPP₁ through GPP₅ represent outputs from the five Arctic–Subarctic (AS) adapted formulations. Refer to Sections 3 and 4.1 for a description of each model formulation. ubRMSE and B denote the unbiased root mean squared error and bias, respectively, expressed in gCm⁻²d⁻¹. A positive (negative) B indicates that the model formulation overestimates (underestimates) GPP_{EC}. r is the Pearson correlation coefficient (dimensionless). The evaluation accounts for both spatial and temporal variability. It includes all available GPP_{EC} data points for each ecosystem type after filtering, including those used for calibration (1,650 for upland tundra, 4,632 for taiga forests and 3,653 for wetlands; Section 4.3).

ER	Upland Tundra			Taiga Forests			Wetlands		
	r	ubRMSE	B	r	ubRMSE	B	r	ubRMSE	B
ER _{L4C}	0.43	0.99	0.38	0.33	1.71	-0.11	0.23	1.81	1.76
ER ₁	0.51	0.72	-0.09	0.52	1.28	-0.15	0.49	0.81	-0.06
ER ₂	0.65	0.60	-0.06	0.54	1.23	-0.08	0.53	0.78	-0.02
ER ₃	0.61	0.62	0.00	0.53	1.23	-0.01	0.51	0.79	0.00
ER ₄	0.73	0.53	-0.01	0.59	1.17	0.01	0.51	0.79	-0.03
ER ₅	0.71	0.54	0.00	0.59	1.17	0.02	0.50	0.80	-0.03

Table 5. Same as Table 4, but for **ecosystem respiration (ER)**. The evaluation includes all available ER_{EC} data points for each ecosystem type after filtering, including those used for calibration (1,650 for upland tundra, 4,632 for taiga forests and 3,653 for wetlands; Section 4.3).



NEE	Upland Tundra			Taiga Forests			Wetlands		
	r	ubRMSE	B	r	ubRMSE	B	r	ubRMSE	B
NEE _{L4C}	0.55 (0.44)	0.86 (0.90)	-0.03 (0.06)	0.55 (0.54)	1.17 (1.04)	0.26 (0.40)	0.47 (0.50)	0.99 (0.79)	0.45 (0.73)
NEE _{AS}	0.64 (0.62)	0.73 (0.69)	0.01 (-0.12)	0.63 (0.60)	1.09 (0.97)	0.02 (-0.09)	0.48 (0.33)	0.93 (0.82)	0.01 (0.22)

Table 6. Performance of modeled **net ecosystem CO₂ exchange (NEE)** against daily-averaged eddy covariance (EC) NEE (NEE_{EC}) in upland tundra, taiga forests, and wetlands during the growing season. Modeled NEE is computed as the difference between modeled ecosystem respiration (ER) and gross primary production (GPP). NEE_{L4C} denotes NEE from the original L4C model, while NEE_{AS} refers to outputs from the Arctic–Subarctic (AS) adapted formulations. For upland tundra and taiga forests, NEE_{AS} = ER₄ - GPP₅, while for wetlands NEE_{AS} = ER₃ - GPP₄. The formulation selection was based on their performance scores (Section 4.4). Refer to Sections 3 and 4.1 for a description of each model formulation. ubRMSE and B denote the unbiased root mean squared error and bias, respectively, expressed in gCm⁻²d⁻¹. A positive (negative) B indicates that the model formulation overestimates (underestimates) NEE_{EC}. r is the Pearson correlation coefficient (dimensionless). Values reported outside parentheses represent **spatiotemporal performance**, accounting for both spatial and temporal variability. This evaluation includes all available NEE_{EC} data points for each ecosystem type after filtering (1,650 for upland tundra, 4,632 for taiga forests and 3,653 for wetlands; Section 4.3). Values in parentheses represents **temporal performance**, shown as the median metrics across EC towers.

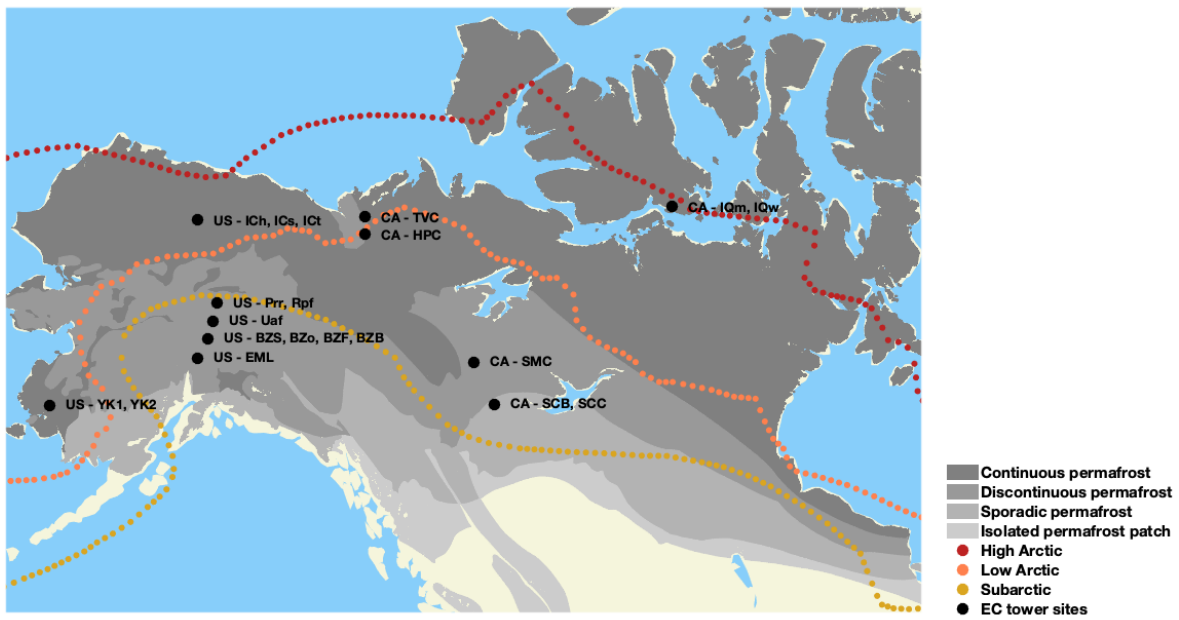


Figure 1. Locations of the 20 eddy covariance (EC) towers providing measurements of net ecosystem exchange (NEE_{EC}), NEE-derived gross primary production (GPP_{EC}) and ecosystem respiration (ER_{EC}) from April 2015 to December 2022. The High Arctic, Low Arctic and Subarctic zones were delineated following the Conservation of Arctic Flora and Fauna (CAFF) working group of the Arctic Council, using Moderate Resolution Imaging Spectroradiometer (MODIS) and Landsat imagery (Potapov et al., 2008). The permafrost extent is estimated in percent areal coverage (Brown et al., 2002): continuous (>90-100% areal extent), discontinuous (>50-90%), sporadic (10-50%) and isolated patches (<10%). Due to overlapping, a single color dot may represent up to four EC towers on the map. Information for each EC tower is listed in Table 1. The figure was inspired by Madelon et al. (2025) and Mavrovic et al. (2023a).

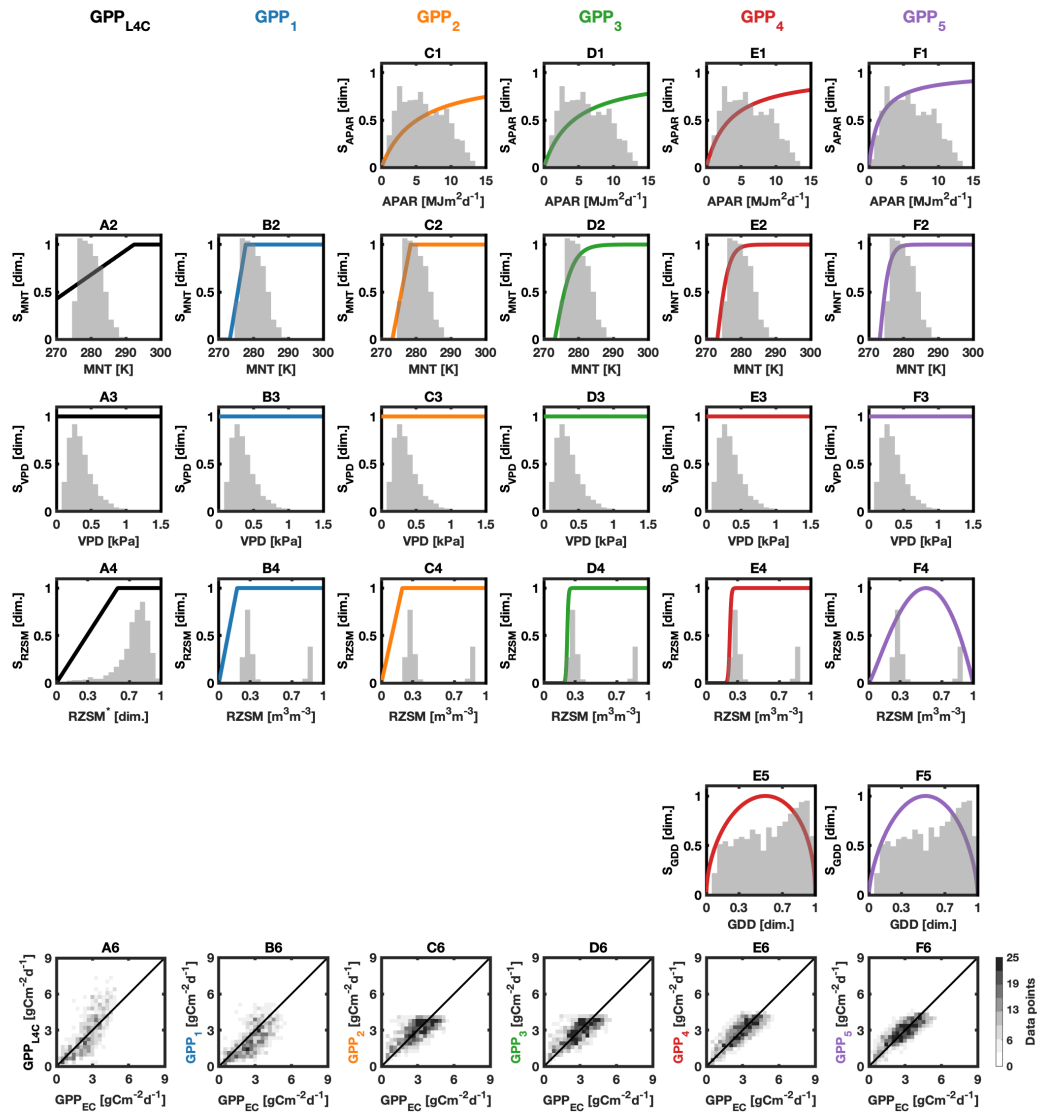


Figure 2. Ecosystem responses used to compute modeled **gross primary production (GPP)** from the L4C model (GPP_{L4C} , column A) and from the Arctic-Subarctic (AS) adapted formulations (GPP_1 through GPP_5 , columns B–F) in **upland tundra** during the growing season. The ecosystem responses are expressed as stress scalars, S_x , for each environmental variable x , where x represents absorbed photosynthetically active radiation (APAR), minimum air temperature (MNT), vapor pressure deficit (VPD), root zone soil moisture (RZSM), and normalized growing degree days (GDD). In the background of each subplot, the histogram of the corresponding environmental variable is shown in light grey. **All ecosystem responses of a given model formulation are calibrated jointly using eddy covariance GPP (GPP_{EC}) as reference, and not based on the histogram values.** In subplot A4, $RZSM^*$ refers to the normalized RZSM used as input in the original L4C model. Subplots A1 and B1 are omitted because APAR is used as a direct input, rather than through a stress scalar, in GPP_{L4C} and GPP_1 formulations. Similarly, subplots A5–D5 are omitted because GDD is not used as input in the GPP_{L4C} , GPP_1 , GPP_2 , and GPP_3 formulations. Refer to Sections 3 and 4.1 for a detailed description of each model formulation. The last row displays scatter plots between modeled GPP against GPP_{EC} . It is a spatiotemporal comparison, accounting for both temporal and spatial variability. It includes all available GPP_{EC} data points for upland tundra after filtering, including those used for calibration (1,650 data points; Section 4.3).

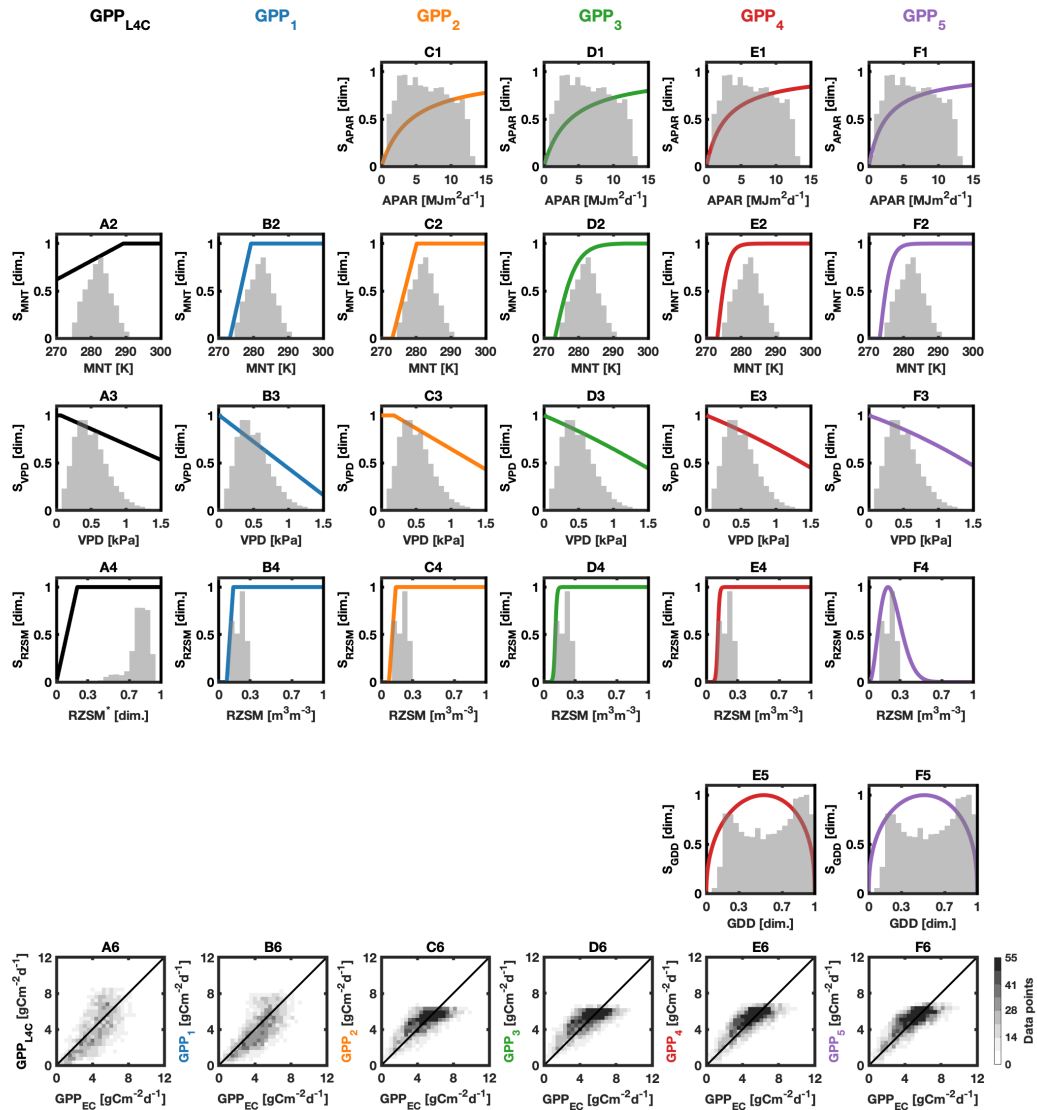


Figure 3. Same as Figure 2, but for **taiga forests**. The spatiotemporal comparison includes all available GPP_{EC} data points for taiga forests after filtering, including those used for calibration (4,632 data points; Section 4.3).

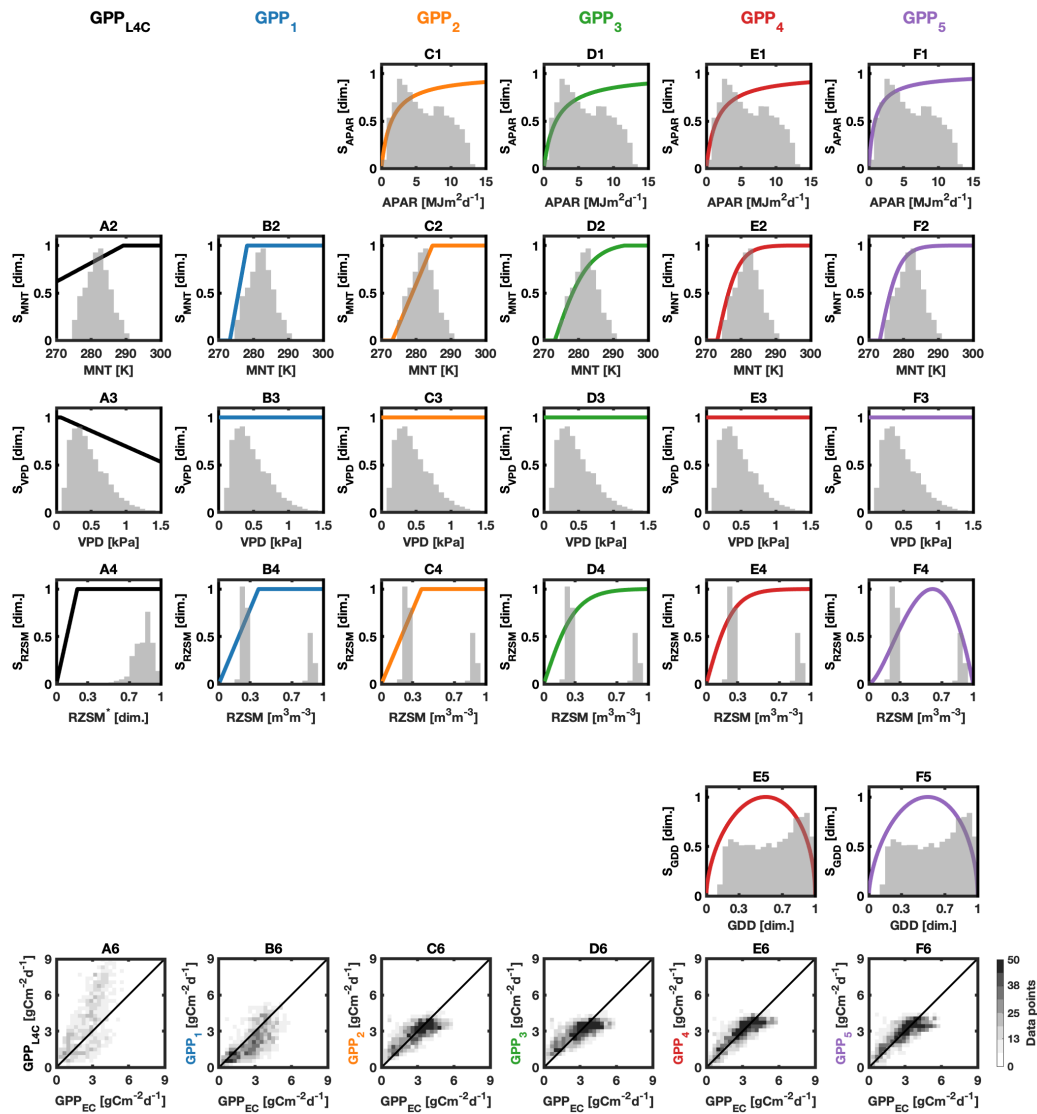


Figure 4. Same as Figure 2, but for wetlands. The spatiotemporal comparison includes all available GPP_{EC} data points for wetlands after filtering, including those used for calibration (3,653 data points; Section 4.3).

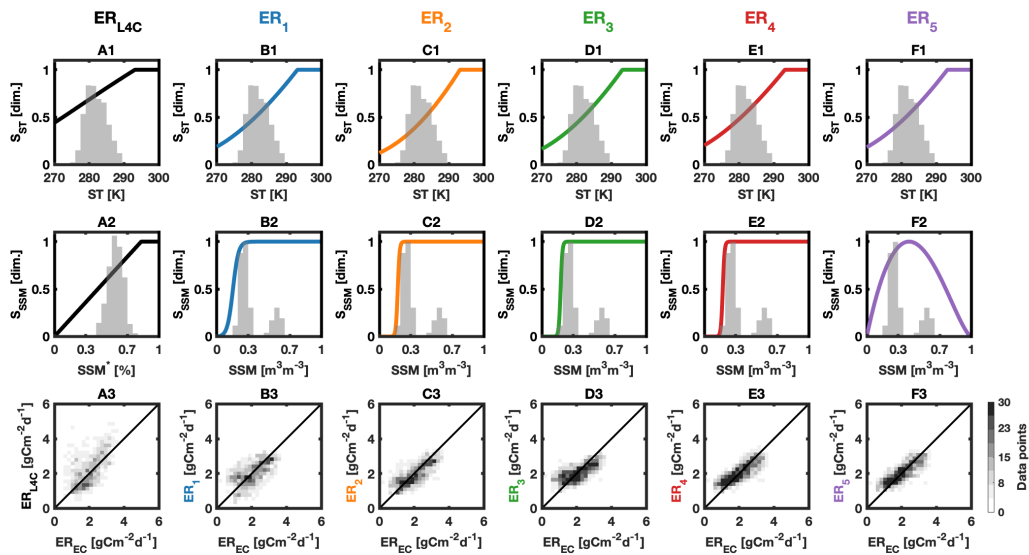


Figure 5. Ecosystem responses used to compute modeled **ecosystem respiration (ER)** from the L4C model (ER_{L4C} , column A) and from the Arctic-Subarctic (AS) adapted formulations (ER_1 through ER_5 , columns B–F) in **upland tundra** during the growing season. The ecosystem responses are expressed as stress scalars, S_x , for each environmental variable x , where x represents soil temperature (ST) and surface soil moisture (SSM). In the background of each subplot, the histogram of the corresponding environmental variable is shown in light grey. **All ecosystem responses of a given model formulation are calibrated jointly using daily-averaged eddy covariance ER (ER_{EC}) as reference, and not based on the histogram values.** In subplot A2, SSM^* refers to the SSM in relative wetness unit used as input in the original L4C model. Refer to Sections 3 and 4.1 for a detailed description of each model formulation. The last row displays scatter plots between modeled ER against ER_{EC} . It is a spatiotemporal comparison, accounting for both temporal and spatial variability. It includes all available ER_{EC} data points for upland tundra after filtering, including those used for calibration (1,650 data points; Section 4.3).

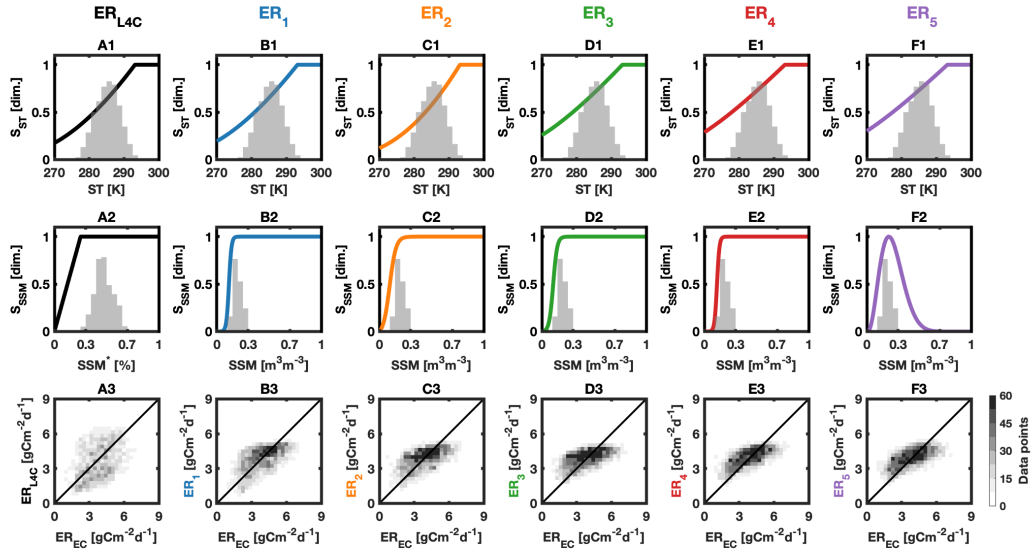


Figure 6. Same as Figure 5, but for **taiga forests**. The spatiotemporal comparison includes all available ER_{EC} data points for taiga forests after filtering, including those used for calibration (4,632 data points; Section 4.3).

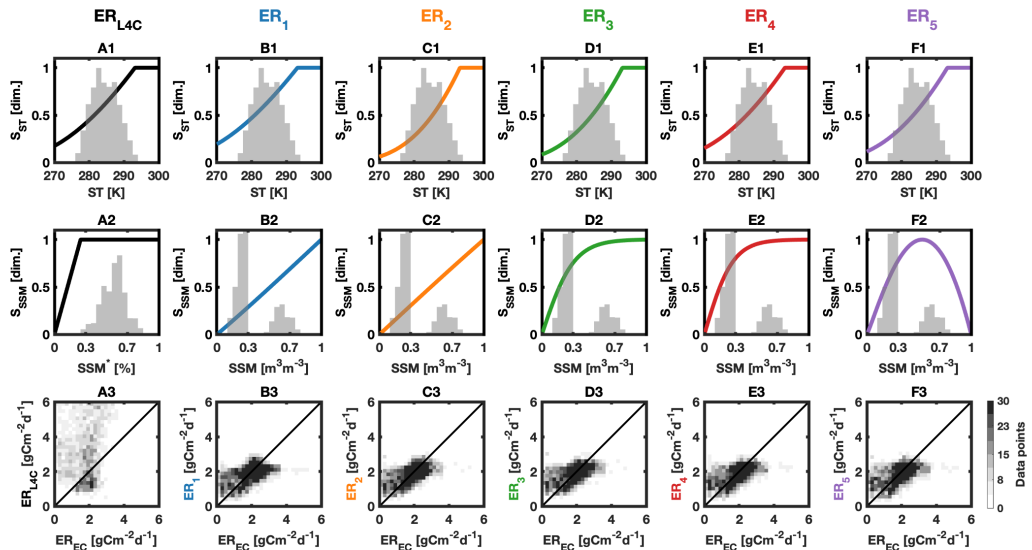


Figure 7. Same as Figure 5, but for **wetlands**. The spatiotemporal comparison includes all available ER_{EC} data points for wetlands after filtering, including those used for calibration (3,653 data points; Section 4.3).

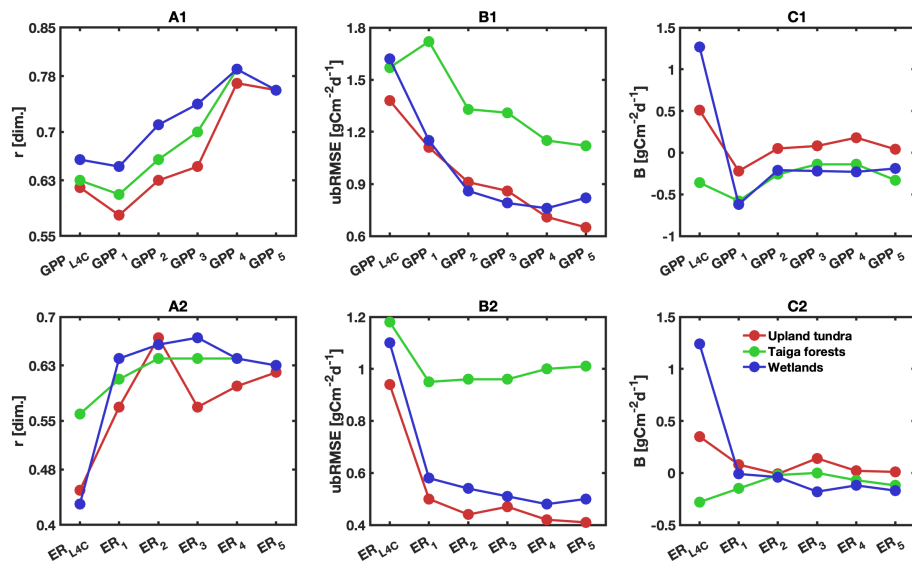


Figure 8. Temporal performance of modeled **gross primary production (GPP)** and **ecosystem respiration (ER)** against daily-averaged eddy covariance GPP (GPP_{EC}) and ER (ER_{EC}) in **upland tundra**, **taiga forests**, and **wetlands** during the growing season. GPP_{L4C} and ER_{L4C} refer to GPP and ER from the original L4C model, while GPP_1 through GPP_5 and ER_1 through ER_5 represent outputs from the Arctic–Subarctic (AS) adapted formulations. Descriptions of the model formulations are provided in Sections 3 and 4.1. $ubRMSE$ and B denote the unbiased root mean squared error and bias, respectively, expressed in $gCm^{-2}d^{-1}$. A positive (negative) B indicates that the model formulation overestimates (underestimates) GPP_{EC} or ER_{EC} . r is the Pearson correlation coefficient (dimensionless). Reported values correspond to the median metric across all EC towers.



655 **Appendix A: Supplementary figure**

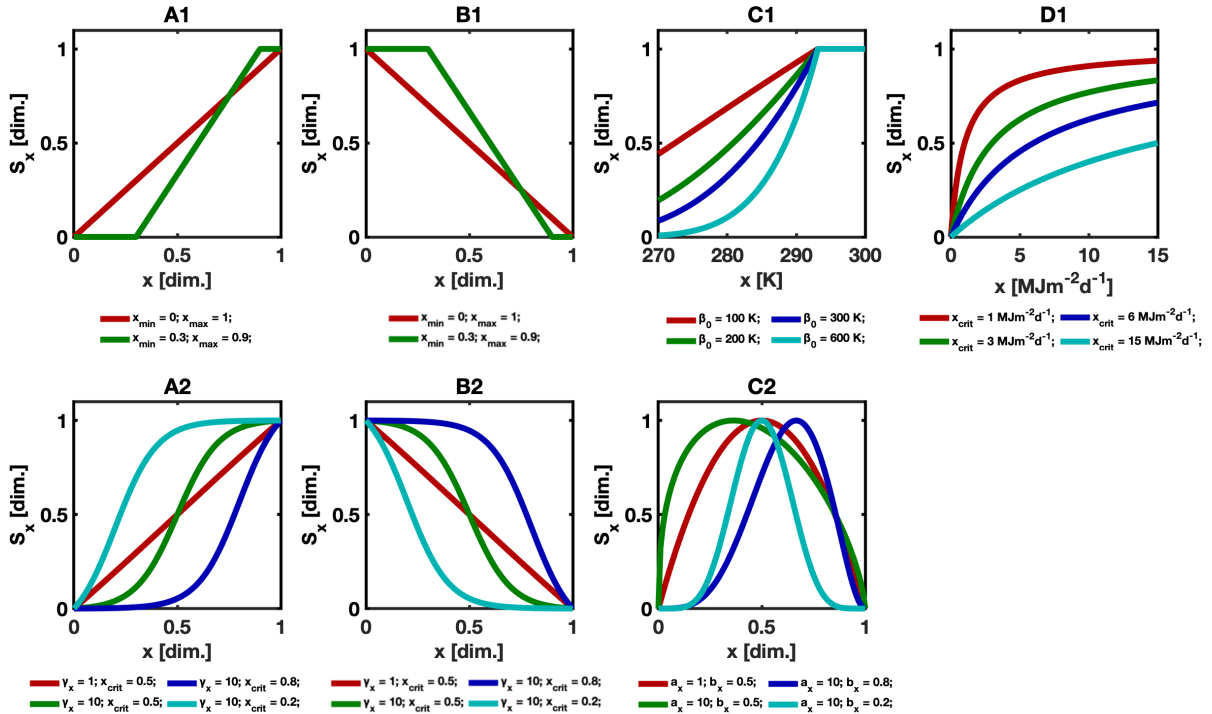


Figure A1. Behavior of the ecosystem response functions used in the L4C model and the Arctic–Subarctic adapted formulations. Each panel shows the same response function evaluated across a range of parameter values to illustrate how parameterization affects function shape. Refer to Sections 3 and 4.1 for a detailed description of each model formulation. Panels A1, B1, and C1 correspond to Equations 7a,c,d 7b, and 7e, respectively; panel D1 corresponds to Equation 8b. Panels A2 and B2 correspond to Equations 9a,c and 9b, respectively; panel C2 corresponds to Equations 10b and 11.



References

Aubinet, M., Vesala, T., and Papale, D.: Eddy covariance: a practical guide to measurement and data analysis, Springer Science & Business Media, 2012.

Baldocchi, D., Falge, E., Gu, L., Olson, R., Hollinger, D., Running, S., Anthoni, P., Bernhofer, C., Davis, K., Evans, R., Fuentes, J., Goldstein, A., Katul, G., Law, B., Lee, X., Malhi, Y., Meyers, T., Munger, W., Oechel, W., Paw U, K., Pilegaard, K., Schmid, H., Valentini, R., Verma, S., Vesala, T., Wilson, K., and Wofsy, S.: FLUXNET: A New Tool to Study the Temporal and Spatial Variability of Ecosystem-Scale Carbon Dioxide, Water Vapor, and Energy Flux Densities., *Am. Meteorol. Soc.*, 82(11), 2415–2434, [https://doi.org/https://doi.org/10.1175/1520-0477\(2001\)082<2415:FANTTS>2.3.CO;2](https://doi.org/https://doi.org/10.1175/1520-0477(2001)082<2415:FANTTS>2.3.CO;2), 2007.

Bao, S., Wutzler, T., Koirala, S., Cuntz, M., Ibrom, A., Besnard, S., Walther, S., Šigut, L., Moreno, A., Weber, U., Wohlfahrt, G., Cleverly, J., Migliavacca, M., Woodgate, W., Merbold, L., Elmar, V., and Carvalhais, N.: Environment-sensitivity functions for gross primary productivity in light use efficiency models, *Agricultural and Forest Meteorology*, 312, 108 708, 2022.

Bell, J., Palecki, M., Baker, C., Collins, W., Lawrimore, J., Leeper, R., Hall, M., Kochendorfer, J., Meyers, T., Wilson, T., and Diamond, H.: U.S. Climate Reference Network soil moisture and temperature observations., *J. Hydrometeorol.*, 14, 977–988, 2013.

Blume-Werry, G., Milbau, A., Teuber, L. M., Johansson, M., and Dorrepaal, E.: Dwelling in the deep—strongly increased root growth and rooting depth enhance plant interactions with thawing permafrost soil, *New Phytologist*, 223, 1328–1339, 2019.

Bowling, D. R., Logan, B. A., Hufkens, K., Aubrecht, D. M., Richardson, A. D., Burns, S. P., Anderegg, W. R. L., Blanken, P. D., and Eiriksson, D. P.: Limitations to winter and spring photosynthesis of a Rocky Mountain subalpine forest, *Agricultural and Forest Meteorology*, 252, 241–255, 2018.

Bracho, R., Celis, G., Rodenhizer, H., See, C., and Schuur, E. A.: AmeriFlux BASE US-EML Eight Mile Lake Permafrost thaw gradient, Healy Alaska, Ver. 4-5, AmeriFlux AMP, (Dataset), <https://doi.org/https://doi.org/10.17190/AMF/1418678>, 2021.

Brown, J., Ferrians, O., Heginbottom, J., and Melnikov, E.: Circum-Arctic Map of Permafrost and Ground-Ice Conditions, Version 2., Boulder, Colorado USA., 2002.

Burba, G.: Eddy covariance method for scientific, industrial, agricultural and regulatory applications: A field book on measuring ecosystem gas exchange and areal emission rates, LI-Cor Biosciences, 2013.

Burba, G.: Eddy covariance method for scientific, regulatory, and commercial applications, LI-COR Biosciences, 2022.

Chapin, F., Woodwell, G., Randerson, J., Rastetter, E., Lovett, G., Baldocchi, D., Clark, D., Harmon, M., Schimel, D., Valentini, R., Wirth, C., Aber, J., Cole, J., Goulden, M., Harden, J., Heimann, M., Howarth, R., Matson, P., McGuire, A., Melillo, J., Mooney, H., Neff, J., Houghton, R., Pace, M., Ryan, M., Running, S., Sala, O., Schlesinger, W., and Schulze, E.-D.: Reconciling Carbon-cycle Concepts, Terminology, and Methods., *Ecosystems*, 9, 1041–1050, 2006.

Chen, N., Zhang, Y., Yuan, F., Song, C., Xu, M., Wang, Q., Hao, G., Bao, T., Zuo, Y., Liu, J., Song, Y., Sun, L., Guo, Y., Zhang, H., Ma, G., Du, Y., Xu, X., and Wang, X.: Warming-induced vapor pressure deficit suppression of vegetation growth diminished in northern peatlands, *Nature Communications*, 14, 7885, 2023.

Churchill, A. C., Turetsky, M. R., McGuire, A. D., and Hollingsworth, T. N.: Response of plant community structure and primary productivity to experimental drought and flooding in an Alaskan fen, *Canadian Journal of Forest Research*, 45, 185–193, 2015.

Colliander, A., Jackson, T., Bindlish, R., Chan, S., Das, N., Kim, S., Cosh, M., Dunbar, R., Dang, L., Pashaian, L., Asanuma, J., Aida, K., Berg, A., Rowlandson, T., Bosch, D., Caldwell, T., Taylor, K., Goodrich, D., al Jassar, H., Lopez-Baeza, E., Martínez Fernández, J., González-Zamora, A., Livingston, S., McNairn, H., Pacheco, A., Moghaddam, M., Montzka, C., Notarnicola, C., Niedrist, G., Pellarin,



695 T., Prueger, J., Pulliainen, J., Rautiainen, K., Ramos, J., Seyfried, M., Starks, P., Su, Z., Zeng, Y., van der Velde, R., Thibeault, M., Dorigo, W., Vreugdenhil, M., Walker, J. P., Wu, X., Monerris, A., O'Neill, P. E., Entekhabi, D., Njoku, E., and Yueha, S.: Validation of SMAP surface soil moisture products with core validation sites, *Remote sensing of environment*, 191, 215–231, 2017.

Crawford, R. M. M.: *Tundra-taiga biology*, Oxford University Press, 2013.

Davis, T. W., Prentice, I. C., Evans, B. J., Wang, H., and Gilbert, X.: The Global ecosystem Production in Space and Time (GePiSaT) Model of the Terrestrial Biosphere, 2014, H53J–04, 2014.

700 Derksen, C., Xu, X., Scott Dunbar, R., Colliander, A., Kim, Y., Kimball, J. S., Black, T. A., Eus Kirchen, E., Langlois, A., Loranty, M. M., Marsh, P. and Rautiainen, K., Roy, A., Royer, A., and Stephens, J.: Retrieving landscape freeze/thaw state from Soil Moisture Active Passive (SMAP) radar and radiometer measurements, *Remote Sensing of Environment*, 194, 48–62, 2017.

710 Dragoni, D., Schmid, H. P., Grimmond, C. S. B., and Loescher, H. W.: Uncertainty of annual net ecosystem productivity estimated using eddy covariance flux measurements, *Journal of Geophysical Research: Atmospheres*, 112, 2007.

705 Endsley, K., Kimball, J., and Reichle, R.: Soil respiration phenology improves modeled phase of terrestrial net ecosystem exchange in northern hemisphere, *Journal of Advances in Modeling Earth Systems*, 14, e2021MS002804, 2022.

Ensminger, I., Sveshnikov, D., Campbell, D. A., Funk, C., Jansson, S., Lloyd, J., Shibistova, O., and Öquist, G.: Intermittent low temperatures constrain spring recovery of photosynthesis in boreal Scots pine forests, *Global Change Biology*, 10, 995–1008, 2004.

715 Entekhabi, D., Njoku, E. G., O'Neill, P. E., Kellogg, K. H., Crow, W. T., Edelstein, W. N., Entin, J. K., Goodman, S. D., Jackson, T. J., Johnson, J., Kimball, J., Piepmeier, J. R., Koster, R. D., Martin, N., McDonald, K. C., Moghaddam, M., Moran, S., Reichle, R., Shi, J. C., Spencer, M. W., Thurman, S. W., Tsang, L., and Van Zyl, J.: The soil moisture active passive (SMAP) mission, *Proceedings of the IEEE*, 98, 704–716, 2010.

Entekhabi, D., Yueh, S., O'Neill, P. E., and Kellogg, K. H.: SMAP Handbook, Tech. rep., Jet Propulsion Laboratory, NASA, 2014.

Eugster, W., McFadden, J. P., and Chapin, F. S.: A comparative approach to regional variation in surface fluxes using mobile eddy correlation towers, *Boundary-Layer Meteorology*, 85, 293–307, 1997.

720 715 Eus Kirchen, E.: AmeriFlux BASE US-BZB Bonanza Creek Thermokarst Bog, Ver. 4-5, AmeriFlux AMP, (Dataset), <https://doi.org/https://doi.org/10.17190/AMF/1773401>, 2022a.

Eus Kirchen, E.: AmeriFlux BASE US-BZF Bonanza Creek Rich Fen, Ver. 4-5, AmeriFlux AMP, (Dataset), <https://doi.org/https://doi.org/10.17190/AMF/1756433>, 2022b.

Eus Kirchen, E.: AmeriFlux BASE US-BZo Bonanza Creek Old Thermokarst Bog, Ver. 3-5, AmeriFlux AMP, (Dataset), <https://doi.org/https://doi.org/10.17190/AMF/1846662>, 2022c.

725 Eus Kirchen, E.: AmeriFlux BASE US-BZS Bonanza Creek Black Spruce, Ver. 3-5, AmeriFlux AMP, (Dataset), <https://doi.org/https://doi.org/10.17190/AMF/1756434>, 2022d.

Eus Kirchen, E., Shaver, G., and Bret-Harte, S.: AmeriFlux BASE US-ICh Imnavait Creek Watershed Heath Tundra, Ver. 4-5, AmeriFlux AMP, (Dataset), <https://doi.org/https://doi.org/10.17190/AMF/1246133>, 2022a.

Eus Kirchen, E., Shaver, G., and Bret-Harte, S.: AmeriFlux BASE US-ICs Imnavait Creek Watershed Wet Sedge Tundra, Ver. 7-5, AmeriFlux AMP, (Dataset), <https://doi.org/https://doi.org/10.17190/AMF/1246130>, 2022b.

Eus Kirchen, E., Shaver, G., and Bret-Harte, S.: AmeriFlux BASE US-ICt Imnavait Creek Watershed Tussock Tundra, Ver. 5-5, AmeriFlux AMP, (Dataset), <https://doi.org/https://doi.org/10.17190/AMF/1246131>, 2022c.

730 Eus Kirchen, E. S., McGuire, A. D., Chapin III, F. S., Yi, S., and Thompson, C. C.: Changes in vegetation in northern Alaska under scenarios of climate change, 2003–2100: implications for climate feedbacks, *Ecological applications*, 19, 1022–1043, 2009.



Falge, E., Baldocchi, D., Olson, R., Anthoni, P., Aubinet, M., Bernhofer, C., Burba, G., Ceulemans, R., Clement, R., Dolman, H., and Granier, A.: Gap filling strategies for defensible annual sums of net ecosystem exchange, *Agricultural and forest meteorology*, 107, 43–69, 2001.

Finkelstein, P. L. and Sims, P. F.: Sampling error in eddy correlation flux measurements, *Journal of Geophysical Research: Atmospheres*, 106, 3503–3509, 2001.

735 Fisher, J. B., Hayes, D. J., Schwalm, C. R., Huntzinger, D. N., Stofferahn, E., Schaefer, K. and Luo, Y., Wullschleger, S. D., Goetz, S., Miller, C. E., Griffith, P., Chadburn, S., Chatterjee, A., Ciais, P., Douglas, T., Genet, H., Ito, A., Neigh, C., Poulter, B., Rogers, B., Sonnentag, O., Tian, H., Wang, W., Xue, Y., Yang, Z.-L., Zeng, N., and Zhang, Z.: Missing pieces to modeling the Arctic-Boreal puzzle, *Environmental Research Letters*, 13, 020 202, 2018.

740 Forkel, M., Carvalhais, N., Rödenbeck, C., Keeling, R., Heimann, M., Thonicke, K., Zachle, S., and Reichstein, M.: Enhanced seasonal CO₂ exchange caused by amplified plant productivity in northern ecosystems, *Science*, 351, 696–699, 2016.

Foster, K. T., Sun, W., Merder, J., Kurz, W., Sinha, E., Nesdoly, A., Metsaranta, J., Hararuk, O., Bond-Lamberty, B. P., Schwalm, C., Natali, S., Huntzinger, D. N., and Michalak, A.: Permafrost, Peatland and Agricultural Regions Key to Reconciling Top-Down and Bottom-Up Estimates of North American Carbon Uptake, in: AGU Fall Meeting Abstracts, vol. 2024, pp. A43T-08, 2024.

745 Fotou Makouate, H. and Zude-Sasse, M.: Advances in Growing Degree Days Models for Flowering to Harvest: Optimizing Crop Management with Methods of Precision Horticulture—A Review, *Horticulturae*, 11, 1415, 2025.

Friedl, M. and Sulla-Menashe, D.: MCD12Q1 MODIS/Terra+Aqua Land Cover Type Yearly L3 Global 500m SIN Grid V006, <https://doi.org/10.5067/MODIS/MCD12Q1.006>, 2019.

Fu, Y. H., Piao, S., Zhao, H., Jeong, S.-J., Wang, X., Vitasse, Y., Ciais, P., and Janssens, I. A.: Unexpected role of winter precipitation in determining heat requirement for spring vegetation green-up at northern middle and high latitudes, *Global change biology*, 20, 3743–3755, 2014.

750 Gelaro, R., McCarty, W., Suárez, M. J., Todling, R., Molod, A., Takacs, L., Randles, C. A., Darmenov, A., Bosilovich, M. G., Reichle, R., Wargan, K., Coy, L., Cullather, R., Draper, C., Akella, S., Buchard, V., Conaty, A., da Silva, A. M., Gu, W., Kim, G.-K., Koster, R., Lucchesi, R., Merkova, D., Nielsen, J. E., Partyka, G., Pawson, S., Putman, W., Rienecker, M., Schubert, S. D., Sienkiewicz, M., and Zhao, B.: The modern-era retrospective analysis for research and applications, version 2 (MERRA-2), *Journal of climate*, 30, 5419–5454, 2017.

755 Gilmanov, T. G., Verma, S. B., Sims, P. L., Meyers, T. P., Bradford, J. A., Burba, G. G., and Suyker, A. E.: Gross primary production and light response parameters of four Southern Plains ecosystems estimated using long-term CO₂-flux tower measurements, *Global Biogeochemical Cycles*, 17, 2003.

Gonsamo, A., Chen, J. M., and D'Odorico, P.: Deriving land surface phenology indicators from CO₂ eddy covariance measurements, *Eco-760 logical Indicators*, 29, 203–207, 2013.

Hagedorn, F., Imboden, J., Moiseev, P. A., Gao, D., Frossard, E., Schleppi, P., Christen, D., Gavazov, K., and Fetzer, J.: Distinct changes in carbon, nitrogen, and phosphorus cycling in the litter layer across two contrasting forest–tundra ecotones, *Biogeosciences*, 22, 2959–2977, 2025.

Hayes, D. J., McGuire, A. D., Kicklighter, D. W., Gurney, K. R., Burnside, T., and Melillo, J. M.: Is the northern high-latitude land-based 765 CO₂ sink weakening?, *Global Biogeochemical Cycles*, 25, 2011.

He, H., Moore, T., Lafleur, P., Sonnentag, O., Humphreys, E., Wu, M., and Roulet, N.: Spring phenology in photosynthesis control and modeling for a temperate bog, *Frontiers in Environmental Science*, 13, 1548 578, 2025.



Heinzelmann, V., Marinissen, J., Aerts, R., Cornelissen, J. H. C., and Bokhorst, S.: Stronger Drought Response of CO₂ Fluxes in Tundra Heath Compared to Sphagnum Peatland in the Sub-Arctic, *Global Change Biology*, 31, e70210, 2025.

770 Helbig, M., Chasmer, L. E., Desai, A. R., Kljun, N., Quinton, W. L., and Sonnentag, O.: Direct and indirect climate change effects on carbon dioxide fluxes in a thawing boreal forest–wetland landscape, *Global Change Biology*, 23, 3231–3248, 2017a.

Helbig, M., Chasmer, L. E., Kljun, N., Quinton, W. L., Treat, C. C., and Sonnentag, O.: The positive net radiative greenhouse gas forcing of increasing methane emissions from a thawing boreal forest-wetland landscape, *Global change biology*, 23, 2413–2427, 2017b.

Hu, F. and Bliss, L.: Tundra, *Encyclopedia Britannica*, <https://www.britannica.com/science/tundra>, [Date accessed: 2025-06-11], 2025.

775 Huang, X., Xiao, J., and Ma, M.: Evaluating the performance of satellite-derived vegetation indices for estimating gross primary productivity using FLUXNET observations across the globe, *Remote Sensing*, 11, 1823, 2019.

Hugelius, G., Strauss, J., Zubrzycki, S., Harden, J., Schuur, E., Ping, C.-L., Schirrmeyer, L., Grosse, G., Michaelson, G., Koven, C., and O'Donnell, J.: Estimated stocks of circumpolar permafrost carbon with quantified uncertainty ranges and identified data gaps, *Biogeosciences*, 11, 6573–6593, 2014.

780 Ise, T. and Moorcroft, P. R.: The global-scale temperature and moisture dependencies of soil organic carbon decomposition: an analysis using a mechanistic decomposition model, *Biogeochemistry*, 80, 217–231, 2006.

Iwahana, G., Kobayashi, H., Ikawa, H., and Suzuki, R.: AmeriFlux BASE US-Prr Poker Flat Research Range Black Spruce Forest, Ver. 4-5, AmeriFlux AMP, (Dataset), <https://doi.org/https://doi.org/10.17190/AMF/1246153>, 2023.

Jia, G. J., Epstein, H. E., and Walker, D. A.: Greening of arctic Alaska, 1981–2001, *Geophysical Research Letters*, 30, 2003.

785 Jones, L., Kimball, J., Reichle, R., Madani, N., Glassy, J., Ardizzone, J., Colliander, A., Cleverly, J., Desai, A., Eamus, D., Euskirchen, E., Hutley, L., Macfarlane, C., and Scott, R.: The SMAP Level 4 Carbon Product for Monitoring Ecosystem Land–Atmosphere CO₂ Exchange., *IEEE T. Geosci. Remote*, 55(11), 6517–6532, <https://doi.org/10.1109/TGRS.2017.2729343>, 2017.

Juday, G.: Taiga, Plants, Animals, Climate, Location, & Facts, *Encyclopedia Britannica*, <https://www.britannica.com/science/taiga>, [Date accessed: 2025-06-11], 2025.

790 Kerr, Y., Waldteufel, P., Richaume, P., Wigneron, J., Ferrazzoli, P., Mahmoodi, A., Al Bitar, A., Cabot, F., Gruhier, C., Juglea, S., Leroux, D., Mialon, A., and Delwart, S.: The SMOS Soil Moisture Retrieval Algorithm, *IEEE Transactions on Geoscience and Remote Sensing*, 50, 1384–1403, <https://doi.org/10.1109/TGRS.2012.2184548>, 2012.

Kim, Y., Kim, S.-D., Enomoto, H., Kushida, K., Kondoh, M., and Uchida, M.: Latitudinal distribution of soil CO₂ efflux and temperature along the Dalton Highway, *Alaska, Polar science*, 7, 162–173, 2013.

795 Kimball, J. S., Jones, L. A., Zhang, K., Heinsch, F. A., McDonald, K. C., and Oechel, W. C.: A Satellite Approach to Estimate Land–Atmosphere CO₂ Exchange for Boreal and Arctic Biomes Using MODIS and AMSR-E, *IEEE Transactions on Geoscience and Remote Sensing*, 47, 569–587, 2008.

Kimball, J. S., Endsley, A., Jones, L. A., Kundig, T., and Reichle, R.: SMAP L4 Global Daily 9 km EASE-Grid Carbon Net Ecosystem Exchange, Version 8, <https://doi.org/10.5067/U7SN8JDZL0UC>, 2025.

800 Kreuzwieser, J., Papadopoulou, E., and Rennenberg, H.: Interaction of flooding with carbon metabolism of forest trees, *Plant Biology*, 6, 299–306, 2004.

Lasslop, G., Reichstein, M., Detto, M., Richardson, A. D., and Baldocchi, D. D.: Comment on Vickers et al.: Self-correlation between assimilation and respiration resulting from flux partitioning of eddy-covariance CO₂ fluxes, *Agricultural and Forest Meteorology*, 150, 312–314, 2010a.



805 Lasslop, G., Reichstein, M., Papale, D., Richardson, A. D., Arneth, A., Barr, A., Stoy, P., and Wohlfahrt, G.: Separation of net ecosystem exchange into assimilation and respiration using a light response curve approach: critical issues and global evaluation, *Global change biology*, 16, 187–208, 2010b.

Leclerc, M. and Thurtell, G.: Footprint prediction of scalar fluxes using a Markovian analysis, *Boundary-Layer Meteorology*, 52, 247–258, 1990.

810 Lees, K., Quaife, T., Artz, R., Khomik, M., and Clark, J.: Potential for using remote sensing to estimate carbon fluxes across northern peatlands—A review, *Science of the Total Environment*, 615, 857–874, 2018.

Lievens, H., Demuzere, M., Marshall, H., Reichle, R. H., Brucker, L., Brangers, I., de Rosnay, P., Dumont, M., Girotto, M., Immerzeel, W. W., Jonas, T., Kim, E., Koch, I., Marty, C., Saloranta, T., Schöber, J., , and De Lannoy, G.: Snow depth variability in the Northern Hemisphere mountains observed from space, *Nature communications*, 10, 4629, 2019.

815 Lloyd, J. and Taylor, J. A.: On the Temperature Dependence of Soil Respiration, *Functional Ecology*, 8, 315–323, <http://www.jstor.org/stable/2389824>, 1994.

López, J., Way, D. A., and Sadok, W.: Systemic effects of rising atmospheric vapor pressure deficit on plant physiology and productivity, *Global Change Biology*, 27, 1704–1720, 2021.

López-Blanco, E., Exbrayat, J., Lund, M., Christensen, T. R., Tamstorf, M. P., Slevin, D., Hugelius, G., Bloom, A. A., and Williams, M.:
820 Evaluation of terrestrial pan-Arctic carbon cycling using a data-assimilation system, *Earth System Dynamics*, 10, 233–255, 2019.

Lucchesi, R.: File Specification for GEOS FP, http://gmao.gsfc.nasa.gov/pubs/office_notes, 2018.

Madelon, R., Kimball, J. S., Endsley, K. A., De Lannoy, G. J. M., Sonnentag, O., Alcock, H., Dett, M., Virkkala, A. M., Rogers, B. M., Watts, J. D., Mavrovic, A., Williamson, S. N., Humphreys, E., Colliander, A., Mialon, A., and Roy, A.: Assessing the SMAP Level-4 Carbon Product over the Arctic and Subarctic Zones, *IEEE Journal of Selected Topics in Applied Earth Observations and Remote Sensing*, 2025.

825 Maire, V., Martre, P., Kattge, J., Gastal, F., Esser, G., Fontaine, S., and Soussana, J.-F.: The coordination of leaf photosynthesis links C and N fluxes in C3 plant species, *PLoS one*, 7, e38345, 2012.

Maltby, E. and Immirzi, P.: Carbon dynamics in peatlands and other wetland soils: Regional and global perspectives, *Chemosphere*, 27, 999–1023, 1993.

Martinez Molera, L.: Machine Learning Q&A: All About Model Validation, MathWorks Online Documentation, <https://www.mathworks.com/campaigns/offers/next/all-about-model-validation.html>, accessed: 2026-01-29, 2025.

830 MathWorks, Inc.: MATLAB R2023b, MathWorks, Natick, Massachusetts, USA, <https://www.mathworks.com/products/matlab.html>, 2023.

Mavrovic, A., Sonnentag, O., Lemmettyinen, J., Baltzer, J. L., Kinnard, C., and Roy, A.: Reviews and syntheses: Recent advances in microwave remote sensing in support of terrestrial carbon cycle science in Arctic-boreal regions, *Biogeosciences*, 20, 2941–2970, 2023a.

Mavrovic, A., Sonnentag, O., Lemmettyinen, J., Voigt, C., Rutter, N., Mann, P., Sylvain, J.-D., and Roy, A.: Environmental controls of winter
835 soil carbon dioxide fluxes in boreal and tundra environments, *Biogeosciences*, 20, 5087–5108, <https://doi.org/10.5194/bg-20-5087-2023>, 2023b.

McCallum, I., Franklin, O., Moltchanova, E., Merbold, L., Schmullius, C., Shvidenko, A., Schepaschenko, D., and Fritz, S.: Improved light and temperature responses for light-use-efficiency-based GPP models, *Biogeosciences*, 10, 6577–6590, <https://doi.org/10.5194/bg-10-6577-2013>, 2013.

840 McGuire, A. D., Christensen, T., Hayes, D., Heroult, A., Euskirchen, E., Kimball, J., Koven, C., Lafleur, P., Miller, P., Oechel, W., Peylin, P., Williams, M., and Yi, Y.: An assessment of the carbon balance of Arctic tundra: comparisons among observations, process models, and atmospheric inversions, *Biogeosciences*, 9, 3185–3204, 2012.



845 McPartland, M. Y., Falkowski, M. J., Reinhardt, J. R., Kane, E. S., Kolka, R., Turetsky, M. R., Douglas, T. A., Anderson, J., Edwards, J. D., Palik, B., and Montgomery, R. A.: Characterizing boreal peatland plant composition and species diversity with hyperspectral remote sensing, *Remote Sensing*, 11, 1685, 2019.

850 Mialon, A., Rodríguez-Fernández, N. J., Santoro, M., Saatchi, S., Mermoz, S., Bousquet, E., and Kerr, Y. H.: Evaluation of the sensitivity of SMOS L-VOD to forest above-ground biomass at global scale, *Remote Sensing*, 12, 1450, 2020.

Mirabel, A., Girardin, M. P., Metsaranta, J., Way, D., and Reich, P. B.: Increasing atmospheric dryness reduces boreal forest tree growth, *Nature Communications*, 14, 6901, 2023.

855 Mishra, U., Hugelius, G., Shelef, E., Yang, Y., Strauss, J., Lupachev, A., Harden, J., Jastrow, J., Ping, C., Riley, W., and Schuur, E.: Spatial heterogeneity and environmental predictors of permafrost region soil organic carbon stocks, *Sci. Adv.*, 7, eaaz5236, 2021.

Myneni, R. and Knyazikhin, Y.: VIIRS/NPP Leaf Area Index/FPAR 8-Day L4 Global 500m SIN Grid V001, <https://doi.org/10.5067/VIIRS/VNP15A2H.001>, 2018.

860 Myneni, R. B., Keeling, C., Tucker, C. J., Asrar, G., and Nemani, R. R.: Increased plant growth in the northern high latitudes from 1981 to 1991, *Nature*, 386, 698–702, 1997.

Natali, S.: AmeriFlux BASE US-YK1 Yukon-Kuskokwim Delta, Izaviknek-Kingaglia uplands, Burned 2015, Ver. 1-5, AmeriFlux AMP, (Dataset.), [https://doi.org/https://doi.org/10.17190/AMF/2331384](https://doi.org/10.17190/AMF/2331384), 2024.

Natali, S.: AmeriFlux BASE US-YK2 Yukon-Kuskokwim Delta, Izaviknek-Kingaglia uplands, Unburned, Ver. 2-5, AmeriFlux AMP, (Dataset.), [https://doi.org/https://doi.org/10.17190/AMF/2331385](https://doi.org/10.17190/AMF/2331385), 2025.

865 Natali, S., Watts, J., Rogers, B., Potter, S., Ludwig, S., Selbmann, A.-K., Sullivan, P., Abbott, B., Arndt, K., Birch, L., Björkman, M., Bloom, A., Celis, G., Christensen, T., Christiansen, C., Commane, R., Cooper, E., Crill, P., Czimczik, C., Davydov, S., Du, J., Egan, J., Elberling, B., Euskirchen, E., Friberg, T., Genet, H., Göckede, M., Goodrich, J., Grogan, P., Helbig, M., Jafarov, E., Jastrow, J., Kalhori, A., Kim, Y., Kimball, J., Kutzbach, L., Lara, M., Larsen, K., Lee, B.-Y., Liu, Z., Loranty, M., Lund, M., Lupascu, M., Madani, N., Malhotra, A., Matamala, R., McFarland, J., McGuire, A., Michelsen, A., Minions, C., Oechel, W., Olefeldt, D., Parmentier, F.-J., Pirk, N., Poulter, B., Quinton, W., Rezanezhad, F., Risk, D., Sachs, T., Schaefer, K., Schmidt, N., Schuur, E., Semenchuk, P., Shaver, G., Sonnentag, O., Starr, G., Treat, C., Waldrop, M., Wang, Y., Welker, J., Wille, C., Xu, Zhang, Z., Zhuang, Q., and Zona, D.: Large loss of CO₂ in winter observed across the northern permafrost region., *Nature Climate Change*, 9, 852–857, 2019.

Natali, S. M., Schuur, E. A., and Rubin, R. L.: Increased plant productivity in Alaskan tundra as a result of experimental warming of soil and permafrost, *Journal of ecology*, 100, 488–498, 2012.

870 Nawaz, A. F., Gargiulo, S., Pichierri, A., and Casolo, V.: Exploring the Role of Non-Structural Carbohydrates (NSCs) Under Abiotic Stresses on Woody Plants: A Comprehensive Review, *Plants*, 14, 328, 2025.

Oechel, W. C., Hastings, S. J., Vourlirtis, G., Jenkins, M., Riechers, G., and Grulke, N.: Recent change of Arctic tundra ecosystems from a net carbon dioxide sink to a source, *Nature*, 361, 520–523, 1993.

Olefeldt, D., Euskirchen, E. S., Harden, J., Kane, E., McGuire, A. D., Waldrop, M. P., and Turetsky, M. R.: A decade of boreal rich fen greenhouse gas fluxes in response to natural and experimental water table variability, *Global change biology*, 23, 2428–2440, 2017.

875 Pallandt, M., Kumar, J., Mauritz, M., Schuur, E., Virkkala, A.-M., Celis, G., Hoffman, F., and Göckede, M.: Representativeness assessment of the pan-Arctic eddy covariance site network and optimized future enhancements., *Biogeosciences*, 19(3), 559–583, <https://doi.org/10.5194/bg-19-559-2022>, 2022.



Parazoo, N. C., Arneth, A., Pugh, T. A. M., Smith, B., Steiner, N., Luus, K., Commane, R., Benmergui, J., Stofferahn, E., Liu, J., Rödenbeck, C., Kawa, R., Euskirchen, E., Zona, D., Arndt, K., Oechel, W., and Miller, C.: Spring photosynthetic onset and net CO₂ uptake in Alaska triggered by landscape thawing, *Global Change Biology*, 24, 3416–3435, 2018.

Peng, J., Tang, J., Xie, S., Wang, Y., Liao, J., Chen, C., Sun, C., Mao, J., Zhou, Q., and Niu, S.: Evidence for the acclimation of ecosystem photosynthesis to soil moisture, *Nature Communications*, 15, 9795, 2024.

Potapov, P., Hansen, M. C., Stehman, S. V., Loveland, T. R., and Pittman, K.: Combining MODIS and Landsat imagery to estimate and map boreal forest cover loss, *Remote sensing of environment*, 112, 3708–3719, 2008.

Prince, M., Roy, A., Royer, A., and Langlois, A.: Timing and spatial variability of fall soil freezing in boreal forest and its effect on SMAP L-band radiometer measurements, *Remote sensing of environment*, 231, 111 230, 2019.

Pu, J., Yan, K., Roy, S., Zhu, Z., Rautiainen, M., Knyazikhin, Y., and Myneni, R. B.: Sensor-independent LAI/FPAR CDR: reconstructing a global sensor-independent climate data record of MODIS and VIIRS LAI/FPAR from 2000 to 2022, *Earth System Science Data Discussions*, 2023, 1–29, 2023.

Pulliainen, J., Aurela, M., Aalto, T., Böttcher, K., Cohen, J., Derksen, C., Heimann, M., Helbig, M., Kolari, P., Kontu, A., Krasnova, A., Launiainen, S., Lemmetyinen, J., Lindqvista, H., Lindroth, A., Lohila, A., Luojusa, K., Mammarella, I., Markkanen, T., Nevala, E., Noe, S., Peichl, M., Pumpanen, J., Rautiainen, K., Salminen, M., Sonnentag, O., Takala, M., Thum, T., Vesala, T., and Vestin, P.: Increase in gross primary production of boreal forests balanced out by increase in ecosystem respiration, *Remote Sensing of Environment*, 313, 114 376, 2024.

Péwé, T.: Permafrost, *Encyclopedia Britannica*, <https://www.britannica.com/science/permafrost>, [Date accessed: 2025-06-11], 2025.

Ramage, J., Kuhn, M., Virkkala, A., Voigt, C., Marushchak, M. E., Bastos, A., Biasi, C., Canadell, J. G., Ciais, P., López-Blanco, E., Natali, S. M., Olefeldt, D., Potter, S., Poulter, B., Rogers, B. M., Schuur, E. A. G., Treat, C., Turetsky, M. R., Watts, J., and Hugelius, G.: The net GHG balance and budget of the permafrost region (2000–2020) from ecosystem flux upscaling, *Global Biogeochemical Cycles*, 38, e2023GB007953, 2024.

Rantanen, M., Karpechko, A. Y., Lipponen, A., Nordling, K., Hyvärinen, O., Ruosteenoja, K., Vihma, T., and Laaksonen, A.: The Arctic has warmed nearly four times faster than the globe since 1979, *Communications Earth & Environment*, 3, 168, 2022.

Rautiainen, K., Parkkinen, T., Lemmetyinen, J., Schwank, M., Wiesmann, A., Ikonen, J., Derksen, C., Davydov, S., Davydova, A., Boike, J., Langer, M., Drusch, M., and Pulliainen, J.: SMOS prototype algorithm for detecting autumn soil freezing, *Remote Sensing of Environment*, 180, 346–360, 2016.

Reichle, R., De Lannoy, G., Koster, R., Crow, W., Kimball, J., Liu, Q., and Bechtold, M.: SMAP L4 Global 9 km EASE-Grid Surface and Root Zone Soil Moisture Land Model Constants, Version 8, <https://doi.org/10.5067/PXQIBL2ALDZD>, 2025.

Reichle, R. H., Liu, Q., Koster, R. D., Crow, W. T., De Lannoy, G. J., Kimball, J. S., Ardizzone, J. V., Bosch, D., Colliander, A., Cosh, M., Kolassa, J., Mahanama, S. P., Prueger, J., Starks, P., and Walker, J. P.: Version 4 of the SMAP level-4 soil moisture algorithm and data product, *Journal of Advances in Modeling Earth Systems*, 11, 3106–3130, 2019.

Reichle, R. H., Liu, Q., Ardizzone, J. V., Bechtold, M., Crow, W. T., De Lannoy, G., Kimball, J. S., and Koster, R. D.: Soil moisture active passive (smap) project assessment report for version 7 of the l4_sm data product, 2023.

Reichstein, M., Falge, E., Baldocchi, D., Papale, D., Aubinet, M., Berbigier, P., Bernhofer, C., Buchmann, N., Gilmanov, T., and Granier, A.: On the separation of net ecosystem exchange into assimilation and ecosystem respiration: review and improved algorithm, *Global change biology*, 11, 1424–1439, 2005.



Robinson, S. D. and Moore, T. R.: The influence of permafrost and fire upon carbon accumulation in high boreal peatlands, Northwest Territories, Canada, Arctic, Antarctic, and Alpine Research, 32, 155–166, 2000.

Rouse, W. R., Douglas, M. S. V., Hecky, R. E., Hershey, A. E., Kling, G. W., Lesack, L., Marsh, P., McDonald, M., Nicholson, B. J., Roulet, N. T., and SMOL, J. P.: Effects of climate change on the freshwaters of arctic and subarctic North America, Hydrological processes, 11, 873–902, 1997.

Runkle, B. R. K., Sachs, T., Wille, C., Pfeiffer, E.-M., and Kutzbach, L.: Bulk partitioning the growing season net ecosystem exchange of CO₂ in Siberian tundra reveals the seasonality of its carbon sequestration strength, Biogeosciences, 10, 1337–1349, <https://doi.org/10.5194/bg-10-1337-2013>, 2013.

Salmabadi, H., Pardo Lara, R., Berg, A., Mavrovic, A., Hanes, C., Montpetit, B., and Roy, A.: Improving Seasonally Frozen Ground Monitoring Using Soil Freezing Characteristic Curve in Permittivity–Temperature Space, EGUsphere, 2025, 1–36, <https://doi.org/10.5194/egusphere-2025-620>, 2025.

Schaefer, K., Schwalm, C. R., Williams, C., Arain, M. A., Barr, A., Chen, J. M., Davis, K. J., Dimitrov, D., Hilton, T. W., Hollinger, D. Y., Humphreys, E., Poulter, B., Racza, B. M., Richardson, A. D., Sahoo, A., Thornton, P., Vargas, R., Verbeeck, H., Anderson, R., Baker, I., Black, T. A., Bolstad, P., Chen, J., Curtis, P. S., Desai, A. R., Dietze, M., Dragoni, D., Gough, C., Grant, R. F., Gu, L., Jain, A., Kucharik, C., Law, B., Liu, S., Lokipitiya, E., Margolis, H. A., Matamala, R., McCaughey, J. H., Monson, R., Munger, J. W., Oechel, W., Peng, C., Price, D. T., Ricciuto, D., Riley, W. J., Roulet, N., Tian, H., Tonitto, C., Torn, M., Weng, E., and X., Z.: A model-data comparison of gross primary productivity: Results from the North American Carbon Program site synthesis, Journal of Geophysical Research: Biogeosciences, 117, 2012.

Schaefer, K., Lantuit, H., Romanovsky, V. E., G., S. E. A., and Witt, R.: The impact of the permafrost carbon feedback on global climate, Environmental Research Letters, 9(8), 085–003, <https://doi.org/10.1088/1748-9326/9/8/085003>, 2014.

Schuepp, P., Leclerc, M., MacPherson, J., and Desjardins, R.: Footprint prediction of scalar fluxes from analytical solutions of the diffusion equation, Boundary-Layer Meteorology, 50, 355–373, 1990.

Schuur, E., Abbott, B., Bowden, W., Brovkin, V., Camill, P., Canadell, J., Chanton, J., Chapin, F., Christensen, T., Ciais, P., Crosby, B. T., Czimczik, C. I., Grosse, G., Harden, J., Hayes, D. J., Hugelius, G., Jastrow, J. D., Jones, J. B., Kleinen, T., Koven, C. D., Krinner, G., Kuhry, P., Lawrence, D. M., McGuire, A. D., Natali, S. M., O'Donnell, J. A., Ping, C. L., Riley, W. J., Rinke, A., Romanovsky, V. E., Sannel, A. B. K., Schädel, C., Schaefer, K., Sky, J., Subin, Z. M., Tarnocai, C., Turetsky, M. R., Waldrop, M. P., Walter Anthony, K. M., Wickland, K. P., Wilson, C. J., and Zimov, S. A.: Expert assessment of vulnerability of permafrost carbon to climate change, Climatic Change, 119, 359–374, 2013.

Sierra, C. A., Ceballos-Núñez, V., Hartmann, H., Herrera-Ramírez, D., and Metzler, H.: Ideas and perspectives: Allocation of carbon from net primary production in models is inconsistent with observations of the age of respired carbon, Biogeosciences, 19, 3727–3738, 2022.

Sonnentag, O.: AmeriFlux BASE CA-SMC Smith Creek, Ver. 1-5, AmeriFlux AMP, (Dataset), <https://doi.org/https://doi.org/10.17190/AMF/1767830>, 2021.

Sonnentag, O. and Marsh, P.: AmeriFlux BASE CA-HPC Havikpak Creek, Ver. 1-5, AmeriFlux AMP, (Dataset), <https://doi.org/https://doi.org/10.17190/AMF/1773392>, 2021a.

Sonnentag, O. and Marsh, P.: AmeriFlux BASE CA-TVC Trail Valley Creek, Ver. 1-5, AmeriFlux AMP, (Dataset), <https://doi.org/https://doi.org/10.17190/AMF/1767831>, 2021b.

Sonnentag, O. and Quinton, W. L.: AmeriFlux BASE CA-SCC Scotty Creek Landscape, Ver. 1-5, AmeriFlux AMP, (Dataset), <https://doi.org/https://doi.org/10.17190/AMF/1480303>, 2018.



Sonnentag, O. and Quinton, W. L.: AmeriFlux BASE CA-SCB Scotty Creek Bog, Ver. 2-5, AmeriFlux AMP, (Dataset).,
955 https://doi.org/https://doi.org/10.17190/AMF/1498754, 2021.

Tarnocai, C., Canadell, J., Schuur, E., Kuhry, P., Mazhitova, G., and Zimov, S.: Soil organic carbon pools in the northern circumpolar
permafrost region, *Global biogeochemical cycles*, 23, 2009.

Treat, C. C., Jones, M. C., Alder, J., and Frolking, S.: Hydrologic controls on peat permafrost and carbon processes: New insights from past
and future modeling, *Frontiers in Environmental Science*, 10, 892 925, 2022.

960 Turetsky, M. R., Kane, E. S., Harden, J. W., Ottmar, R. D., Manies, K. L., Hoy, E., and Kasischke, E. S.: Recent acceleration of biomass
burning and carbon losses in Alaskan forests and peatlands, *Nature Geoscience*, 4, 27–31, 2011.

Turetsky, M. R., Abbott, B. W., Jones, M. C., Anthony, K. W., Olefeldt, D., Schuur, E. A., Grosse, G., Kuhry, P., Hugelius, G., Koven, C.,
Lawrence, D. M., Carolyn, G., Sannel, A. B. K., and McGuire, A. D.: Carbon release through abrupt permafrost thaw, *Nature Geoscience*,
13, 138–143, 2020.

965 Ueyama, M., Iwata, H., and Harazono, Y.: AmeriFlux BASE US-Uaf University of Alaska, Fairbanks, Ver. 11-5, AmeriFlux AMP, (Dataset).,
https://doi.org/https://doi.org/10.17190/AMF/1480322, 2023a.

Ueyama, M., Iwata, H., and Harazono, Y.: AmeriFlux BASE US-Rpf Poker Flat Research Range: Succession from fire scar to deciduous
forest, Ver. 9-5, AmeriFlux AMP, (Dataset)., https://doi.org/https://doi.org/10.17190/AMF/1579540, 2023b.

Valkenborg, B., De Lannoy, G. J. M., Gruber, A., Miralles, D. G., Köhler, P., Frankenbergs, C., Desai, A. R., Humphreys, E., Klatt, J., Lohila,
970 A., Nilsson, M. B., Tuittila, E.-S., and Bechtold, M.: Drought and Waterlogging Stress Regimes in Northern Peatlands Detected Through
Satellite Retrieved Solar-Induced Chlorophyll Fluorescence, *Geophysical Research Letters*, 50, e2023GL105 205, 2023.

Virkkala, A., Aalto, J., Rogers, B. M., Tagesson, T., Treat, C. C., Natali, S. M., Watts, J. D., Potter, S., Lehtonen, A., Mauritz, M., Schuur, E.
A. G., Kochendorfer, J., Zona, D., Oechel, W., Kobayashi, K., Humphreys, E., Goeckede, M., Iwata, H., Lafleur, P. M., Euskirchen, E. S.,
975 Bokhorst, S., Marushchak, M., Martikainen, P. J., Elberling, B., Voigt, C., Biasi, C., Sonnentag, O., Parmentier, F. W., Ueyama, M., Celis,
G., St.Louis, V. L., Emmerton, C. A., Peichl, M., Chi, J., Järveoja, J., Nilsson, M. B., Oberbauer, S. F., Torn, M. S., Park, S., Dolman, H.,
Mammarella, I., Chae, N., Poyatos, R., López-Blanco, E., Christensen, T. R., Kwon, M. J., Sachs, T., Holl, D., and Luoto, M.: Statistical
upscaling of ecosystem CO₂ fluxes across the terrestrial tundra and boreal domain: Regional patterns and uncertainties, *Global Change
Biology*, 27, 4040–4059, 2021.

Virkkala, A., Rogers, B. M., Watts, J. D., Arndt, K. A., Potter, S., Wargowsky, I., Schuur, E. A. G., See, C., Mauritz, M., Boike, J., Bret-
980 Harte, S. M., Burke, E. J., Burrell, A., Chae, N., Chatterjee, A., Chevallier, F., Christensen, T. R., Commane, R., Dolman, H., Elberling,
B., Emmerton, C. A., Euskirchen, E. S., Feng, L., Goeckede, M., Grelle, A., Helbig, M., Holl, D., Järveoja, J., Kobayashi, H., Kutzbach,
L., Liu, J., Liujkx, I., López-Blanco, E., Lunneberg, K., Mammarella, I., Marushchak, M. E., Mastepanov, M., Matsuura, Y., Maximov, T.,
Merbold, L., Meyer, G., Nilsson, M. B., Niwa, Y., Oechel, W., Park, S., Parmentier, F. W., Peichl, M., Peters, W., Petrov, R., Quinton, W.,
Rödenbeck, C., Sachs, T., Schulze, C., Sonnentag, O., St.Louis, V., Tuittila, E., Ueyama, M., Varlagin, A., Zona, D., and Natali, S. M.: An
985 increasing Arctic-Boreal CO₂ sink despite strong regional sources, *bioRxiv*, https://doi.org/10.1101/2024.02.09.579581, 2024.

Wang, F., Chen, J. M., Gonsamo, A., Zhou, B., Cao, F., and Yi, Q.: A two-leaf rectangular hyperbolic model for estimating
GPP across vegetation types and climate conditions, *Journal of Geophysical Research: Biogeosciences*, 119, 1385–1398,
https://doi.org/https://doi.org/10.1002/2013JG002596, 2014a.

Wang, H., Prentice, I. C., and Davis, T. W.: Biophysical constraints on gross primary production by the terrestrial biosphere, *Biogeosciences*,
990 11, 5987–6001, 2014b.



Wang, H., Prentice, I. C., Keenan, T. F., Davis, T. W., Wright, I. J., Cornwell, W. K., Evans, B. J., and Peng, C.: Towards a universal model for carbon dioxide uptake by plants, *Nature plants*, 3, 734–741, 2017.

Wania, R., Ross, I., and Prentice, I. C.: Integrating peatlands and permafrost into a dynamic global vegetation model: 1. Evaluation and sensitivity of physical land surface processes, *Global Biogeochemical Cycles*, 23, 2009.

995 Webb, E. E., Schuur, E. A., Natali, S. M., Oken, K. L., Bracho, R., Krapek, J. P., Risk, D., and Nickerson, N. R.: Increased wintertime CO₂ loss as a result of sustained tundra warming, *Journal of Geophysical Research: Biogeosciences*, 121, 249–265, 2016.

Xiao, X., Jin, C., and Dong, J.: Gross primary production of terrestrial vegetation, in: *Biophysical applications of satellite remote sensing*, pp. 127–148, Springer, 2013.

Xu, B., Park, T., Yan, K., Chen, C., Zeng, Y., Song, W., Yin, G., Li, J., Liu, Q., Knyazikhin, Y., and Myneni, R. B.: Analysis of global 1000 LAI/FPAR products from VIIRS and MODIS sensors for spatio-temporal consistency and uncertainty from 2012–2016, *Forests*, 9, 73, 2018.

Yi, Y., Kimball, J. S., Watts, J. D., Natali, S. M., Zona, D., Liu, J., Ueyama, M., Kobayashi, H., Oechel, W., and Miller, C. E.: Investigating the sensitivity of soil heterotrophic respiration to recent snow cover changes in Alaska using a satellite-based permafrost carbon model, *Biogeosciences*, 17, 5861–5882, 2020.

1005 Zhang, M., Fu, L., Ma, D., Wang, X., and Liu, A.: Effects of Microtopography on Soil Microbial Community Structure and Abundance in Permafrost Peatlands, *Microorganisms*, 12, 867, 2024.

Zona, D., Gioli, B., Commane, R., Lindaas, J., Wofsy, S. C., Miller, C. E., Dinardo, S. J., Dengel, S., Sweeney, C., Karion, A., Chang, R. Y. W., Henderson, J. M., Murphy, P. C., Goodrich, J. P., Moreaux, V., Liljedahl, A., Watts, J. D., Kimball, J. S., Lipson, D. A., and Oechel, W. C.: Cold season emissions dominate the Arctic tundra methane budget, *Proceedings of the National Academy of Sciences*, 113, 40–45, 2010 2016.

Zona, D., Lafleur, P. M., Hufkens, K., Gioli, B., Bailey, B., Burba, G., Euskirchen, E. S., Watts, J. D., Arndt, K. A., Farina, M., Kimball, J. S., Heimann, M., Göckede, M., Pallandt, M., Christensen, T. R., Mastepanov, M., López-Blanco, E., Dolman, A. J., Commane, R., Miller, C. E., Hashemi, J., Kutzbach, L., Holl, D., Boike, J., Wille, C., Sachs, T., Kalhor, A., Humphreys, E. R., Sonnentag, O., Meyer, G., Gosselin, G. H., Marsh, P., and C., O. W.: Pan-Arctic soil moisture control on tundra carbon sequestration and plant productivity, *Global 1015 Change Biology*, 29, 1267–1281, 2023.